

Three Dimensional Hydrodynamic Simulations of Multiphase Galactic Disks with Star Formation Feedback: II. Synthetic H I 21 cm Line Observations

Chang-Goo Kim¹, Eve C. Ostriker¹, and Woong-Tae Kim²

¹*Department of Astrophysical Sciences, Princeton University, Princeton, NJ, 08544, USA*

`cgkim@astro.princeton.edu, eco@astro.princeton.edu`

²*Center for the Exploration of the Origin of the Universe (CEOU), Astronomy Program, Department of Physics & Astronomy, Seoul National University, Seoul 151-742, Republic of Korea*

`wkim@astro.snu.ac.kr`

ABSTRACT

We use three-dimensional numerical hydrodynamic simulations of the turbulent, multiphase atomic interstellar medium (ISM) to construct and analyze synthetic H I 21 cm emission and absorption lines. Our analysis provides detailed tests of 21 cm observables as physical diagnostics of the atomic ISM. In particular, we construct (1) the “observed” spin temperature, $T_{s,\text{obs}}(v_{\text{ch}}) \equiv T_B(v_{\text{ch}})/[1 - e^{-\tau(v_{\text{ch}})}]$, and its optical-depth weighted mean $T_{s,\text{obs}}$; (2) the absorption-corrected “observed” column density, $N_{\text{H,obs}} \propto \int dv_{\text{ch}} T_B(v_{\text{ch}}) \tau(v_{\text{ch}})/[1 - e^{-\tau(v_{\text{ch}})}]$; and (3) the “observed” fraction of cold neutral medium (CNM), $f_{c,\text{obs}} \equiv T_c/T_{s,\text{obs}}$ for T_c the CNM temperature; we compare each observed parameter with true values obtained from line-of-sight (LOS) averages in the simulation. Within individual velocity channels, $T_{s,\text{obs}}(v_{\text{ch}})$ is within a factor 1.5 of the true value up to $\tau(v_{\text{ch}}) \sim 10$. As a consequence, $N_{\text{H,obs}}$ and $T_{s,\text{obs}}$ are respectively within 5% and 12% of the true values for 90% and 99% of LOSs. The optically thin approximation significantly underestimates N_{H} for $\tau > 1$. Provided that T_c is constrained, an accurate observational estimate of the CNM mass fraction can be obtained down to 20%. We show that $T_{s,\text{obs}}$ cannot be used to distinguish the relative proportions of warm and thermally-unstable atomic gas, although the presence of thermally-unstable gas can be discerned from 21 cm lines with $200 \text{ K} \lesssim T_{s,\text{obs}}(v_{\text{ch}}) \lesssim 1000 \text{ K}$. Our mock observations successfully reproduce and explain the observed distribution of the brightness temperature, optical depth, and spin temperature in Roy et al. (2013a). The threshold column density for CNM seen in observations is also reproduced by our mock observations. We explain this observed threshold behavior in terms of vertical equilibrium in the local Milky Way’s ISM disk.

Subject headings: hydrodynamics — methods: numerical — ISM: lines and bands — radio lines: ISM

1. INTRODUCTION

The H I 21 cm line is a powerful tool for studying the atomic interstellar medium (ISM). The first detections of emission and absorption at 21 cm date back to the 1950s (Ewen & Purcell 1951; Muller & Oort 1951 for emission, and Hagen et al. 1955 for absorption). The H I 21 cm line has been observed extensively since then, and proved extremely valuable in revealing many properties of the Milky Way Galaxy, including the vertical and radial distribution and warp of the atomic disk, the galactic rotation curve and dark matter distribution, and spiral structure. In addition to large-scale properties of the Milky Way, H I 21 cm observations provide a wealth of knowledge regarding the detailed physical state of the interstellar medium (see reviews including Burton 1976; Dickey & Lockman 1990; Kalberla & Kerp 2009 and references therein). Recently, the combined Leiden-Argentine-Bonn survey (LAB survey, Kalberla et al. 2005) produced a high-sensitivity 21 cm emission map over the entire sky with 36 arcmin resolution by merging the Leiden-Dwingeloo survey (Hartmann & Burton 1997) with the Instituto Argentino de Radioastronomía survey (Bajaja et al. 2005). This high-sensitivity, single-dish survey with stray radiation correction enables highly detailed investigation of H I in the Milky Way (Levine et al. 2006a,b; Kalberla et al. 2007; Kalberla & Dedes 2008).

Information about the thermodynamic state of hydrogen can be obtained from emission/absorption line pairs, which yield the excitation temperature (a.k.a. spin temperature) of the 21 cm line. Since the available radio continuum background sources are generally weak at 21 cm, the line profile toward a continuum source gives a mixture of emission and absorption by H I. In order to separate emission and absorption, H I emission contributions must be estimated from off-source measurements with sufficient spatial resolution. Using the largest single dish telescope, the Arecibo telescope (beamwidth of 3.2 arcmin), Heiles & Troland (2003a) have investigated the emission/absorption line pairs toward continuum sources at high and intermediate latitudes, but the resolution from a single dish is not sufficient for accurate interpolated emission at latitudes below 10° . Interferometric surveys including the Canadian Galactic Plane Survey (CGPS, Taylor et al. 2003), the Southern Galactic Plane Survey (SGPS, McClure-Griffiths et al. 2005), and the VLA Galactic Plane Survey (VGPS, Stil et al. 2006) achieve angular resolution about ~ 1 arcmin. In order to overcome inherent low sensitivity of interferometric observations to extended structures (zero-spacing), these new surveys apply short-spacing corrections from single dish observations, allowing accurate measurement of the expected emission and hence absorption spectra (Stil et al. 2006). The resulting emission/absorption line pairs in these Galactic plane surveys reveal a pervasive multiphase structure in the atomic ISM out to a galactocentric radius of 25 kpc (Dickey et al. 2009).

Using emission/absorption line pairs, the total atomic column density and the harmonic mean spin temperature on a given line-of-sight (LOS) can be derived with a simple radiative transfer calculation (Spitzer 1978; Draine 2011, see Section 2.3 below). In classical models of the neutral ISM, two distinct phases are expected: the cold neutral medium (CNM; $T \sim 100$ K) and the warm neutral medium (WNM; $T \sim 8000$ K), in pressure equilibrium with each other (e.g., Field et al. 1969; Wolfire et al. 1995, 2003). Since the WNM is optically thin at 21 cm due to its low density and high

temperature, a simple single temperature approximation for radiative transfer would be satisfied if there is no overlap between CNM clouds within narrow velocity channels. However, recent dynamical models that simulate the atomic ISM (e.g., Vázquez-Semadeni et al. 2000; Audit & Hennebelle 2005; Mac Low et al. 2005; Hennebelle & Audit 2007; Piontek & Ostriker 2007; Kim et al. 2008; Seifried et al. 2011; Saury et al. 2013), along with detailed observations (e.g., Heiles & Troland 2003b; Kanekar et al. 2003; Roy et al. 2013b) have shown a broad distribution over a wide temperature range and a significant amount of gas in the thermally unstable temperature range $T = 500 - 5000$ K (Wolfire et al. 1995). Moreover, the velocity field is complex, with turbulence dominated by large scales but potential for velocity overlap at distinct locations along LOSs.

Under realistic circumstances of complex velocity fields and broad temperature distributions, validity of the standard assumptions adopted in interpreting H I observations are open to question. To address some of these questions, Chengalur et al. (2013) have performed Monte Carlo simulations assigning varying mass fractions of each component along each LOS, showing that the isothermal estimator of the H I column density agrees well with the true column density within a factor of 2. However, to date there have been no corresponding studies that construct and analyze synthetic emission/absorption lines using results from realistic hydrodynamic simulations of the ISM. In this paper, we utilize our recent three dimensional hydrodynamic simulations (Kim et al. 2013, hereafter Paper I) to create and analyze detailed synthetic H I 21 cm lines. Our simulations enable us to investigate fundamental questions related to use of H I 21 cm lines as ISM diagnostics.

In addition, we can address a puzzle that has emerged from recent deep, high-resolution interferometric observations toward radio loud quasars (Roy et al. 2013a), in combination with the LAB survey. These observations have sufficient sensitivity to detect absorption by the WNM, as in Kanekar et al. (2003). Using emission/absorption line pairs, Kanekar et al. (2011) reported a threshold H I column density at $N_{\text{H,lim}} \equiv 2 \times 10^{20} \text{ cm}^{-2}$, below which the mean spin temperature exceeds $T_s > 1000$ K. They speculated that this apparent threshold might represent a minimum column density for CNM to develop due to self-shielding against ultraviolet photons. However, detailed modeling of interstellar radiation sources have suggested that the ionization fraction remains small for the hydrogen density of $n > 10 \text{ cm}^{-3}$ when the absorbing WNM column density exceeds 10^{18} cm^{-2} for solar neighborhood condition (see Figure 3(c) in Wolfire et al. 1995). In addition, absorption lines with a low optical depth and a narrow line width have been detected, implying a very low CNM column density of $N_{\text{H}} \sim 5 \times 10^{18} \text{ cm}^{-2}$ (Begum et al. 2010b). Furthermore, Dickey et al. (2009) have shown that the ratio of (integrated) emission to absorption is nearly constant over the radial distance range of 10 to 25 kpc, whereas the emission and absorption alone decrease by two orders of magnitude. This implies that the mass fraction of the CNM is unchanged, while the total column density drops by more than an order of magnitude, lower than $N_{\text{H,lim}}$.

Here, we shall propose an alternative explanation for the H I threshold behavior observed in the solar neighborhood. This proposal is based on the concept of the warm/cold ISM representing a self-regulated thermal and dynamical equilibrium system that is heated and dynamically stirred by energy injection from star formation (Ostriker et al. 2010; Kim et al. 2011). In dynamical equi-

librium, a given midplane pressure implies a minimum column of gas; here, we shall show that this can give rise to a threshold column behavior similar to that seen in observations.

The plan of this paper is as follows. Section 2 briefly reviews the numerical models and explains how we extract LOS simulated data and produce synthetic lines, including our procedure for spin temperature calculation. In Section 3, we compare true values of column density, spin temperature, and CNM mass fraction to those that would be deduced using standard observational methods applied to our synthetic 21 cm lines. Section 4 presents mock observations for brightness temperature, optical depth, and spin temperature for each velocity channel and for column density distributions. We shall show that the mock observations reproduce H I 21 cm line observations very well for individual velocity channels (Roy et al. 2013a) as well as integrated over velocity (Kanekar et al. 2011). In addition, we show that the threshold column density is well reproduced, and consistent with the expectation of the thermal/dynamical model.

2. Numerical Models and Synthetic H I Line Observations

2.1. Brief Review of Numerical Models

In this paper, we utilize recent three dimensional hydrodynamic simulations of multiphase, turbulent galactic disks presented in Paper I to investigate synthetic 21 cm lines. Our numerical models represent a local patch of a galactic disk including galactic differential rotation, external gravity from stars and dark matter, gaseous self-gravity, interstellar cooling and heating, and star formation feedback. We treat star formation feedback to the neutral ISM in two ways. To represent the radiative stage of expanding supernova remnants, we inject radial momentum, which drives turbulence at a wide range of scale. We also apply (spatially-uniform) heating at a rate proportional to the recent star formation rate (SFR), to model far-ultraviolet (FUV) emission. While simplified, this treatment incorporates both thermal and turbulent energy feedback, both of which are required to regulate the ISM properties and SFR properly. The reader is referred to Paper I for complete descriptions of model setup, numerical methods, and detailed evolution. Here, we briefly summarize the dynamical behavior and physical properties of the disk when it has reached a quasi-equilibrium state.

In equilibrium, the disk models contain highly turbulent gas at a wide range of temperatures. CNM clouds tend to settle to the midplane, where they collect to form more massive gravitationally bound clouds (GBCs). Star formation in these GBCs produces feedback that heats the disk and drives expanding SN shells. Shell expansion and heating puff up the disk vertically, reducing the mean density and rate of GBC formation. Fewer GBCs leads to lower SFR and less feedback, until gas settles to the midplane and begins a new cycle of star formation. After an initial transient, the models reach a state characterized by quasi-periodic fluctuations with period¹ of

¹ The natural frequency of the midplane-crossing mode is $\omega_{\text{ver}} \sim \sqrt{4\pi G \rho_{\text{sd}}}$, but because gas streams collide at the

$t_{\text{osc}} \sim 0.5\sqrt{\pi/G\rho_{\text{sd}}}$, where ρ_{sd} is the midplane volume density of stars and dark matter.

After a saturated state is reached, the thermal and dynamical equilibrium model proposed by Ostriker et al. (2010) and Ostriker & Shetty (2011) describes average disk properties very well (see also Kim et al. 2011; Shetty & Ostriker 2012, Paper I). The balance between cooling and heating sets the mean midplane thermal pressure P_{th} to a level between the minimum pressure for the CNM, P_{min} , and the maximum pressure for the WNM, P_{max} (see Wolfire et al. 2003). Ostriker et al. (2010) assumed that P_{th} is approximately equal to the geometric mean value $P_{\text{two}} \equiv \sqrt{P_{\text{min}}P_{\text{max}}}$, which is proportional to the heating rate. Photoelectric heating by FUV radiation, believed to be the dominant heating process for the diffuse ISM (Wolfire et al. 1995, 2003), is proportional to the mean FUV radiation field and hence to the SFR surface density, Σ_{SFR} . We find the approximation $P_{\text{th}} \sim P_{\text{two}}$ holds within 60% in our numerical simulations.

Turbulent driving and dissipation are also expected to be balanced, resulting in the midplane turbulent pressure $P_{\text{turb}} \sim P_{\text{driv}} \equiv 0.25(p_*/m_*)\Sigma_{\text{SFR}}$, where p_* and m_* are respectively the total radial momentum injected to the ISM by a single SN, and total mass in stars per SN (Ostriker & Shetty 2011). Our numerical simulations confirm that $P_{\text{turb}} \sim P_{\text{driv}}$. The total (turbulent plus thermal) midplane pressure is then approximately linearly proportional to Σ_{SFR} . In addition, the total midplane pressure must match the vertical gravitational weight in order to satisfy vertical dynamical equilibrium (e.g., Piontek & Ostriker 2007; Koyama & Ostriker 2009; Kim et al. 2010; Hill et al. 2012). The level of the SFR in equilibrium is self-regulated such that all these constraints are simultaneously satisfied. When the vertical gravitational field is dominated by that of stars (plus dark matter), the equilibrium model predicts $\Sigma_{\text{SFR}} \propto P_{\text{th}} \propto P_{\text{tot}} \propto \Sigma\sqrt{\rho_{\text{sd}}}$, where Σ is the gaseous surface density; our simulations show this is satisfied (Ostriker et al. 2010; Kim et al. 2011, Paper I). This situation is expected to hold for atomic-dominated regions in most galactic disks.

Paper I presents results from 3D simulations at varying Σ . Other model parameters are set as $\rho_{\text{sd}} \propto \Sigma^2$ and $\Omega \propto \Sigma$. The midplane volume density of stars and dark matter is $\rho_{\text{sd}} = 0.05 \text{ M}_{\odot} \text{ pc}^{-3}(\Sigma/10 \text{ M}_{\odot} \text{ pc}^{-2})^2$, and the angular velocity at the center of the local galactic patch is $\Omega = 28 \text{ km s}^{-1} \text{ kpc}^{-1}(\Sigma/10 \text{ M}_{\odot} \text{ pc}^{-2})$. Table 1 summarizes model input parameters and selected, time-averaged physical quantities from the 3D models of Paper I. Column (1) gives the name of each model from Paper I. Column (2) gives the gas surface density Σ . Columns (3) to (5) give selected properties measured in the simulations averaged over one orbital time after saturation: the SFR surface density Σ_{SFR} , the midplane thermal pressure, and the scale height of the WNM, respectively. We list the expected column density of the WNM-only LOS, N_{WNM} , in Column (6) using Equation (21).

midplane, $t_{\text{osc}} \sim \pi/\omega_{\text{ver}}$.

2.2. “Observing” Simulation Output

In order to construct synthetic 21 cm lines analogous to observations of the Milky Way Galaxy, we assume an observer sitting at $(x, y, z) = (0, 0, 0)$, the center of the simulation domain. The Galactic center is located toward the $-x$ direction and the $z = 0$ plane represents the midplane of the Galactic disk. We use the QA10 model, a solar neighborhood analogue. This virtual observer conducts mock observations 10^4 times toward random LOSs of (l, b) distributed uniformly in dl and $d(\sin b)$ to ensure uniform sampling per unit solid angle. Here, the galactic longitude l is measured counterclockwise from the $-x$ axis in the $z = 0$ plane, and the galactic latitude b is measured from the midplane at $z = 0$. As we briefly described in §2.1 (see also Paper I), the model disk suffers quasi-periodic evolutionary cycles with period $t_{\text{osc}} \sim 0.27t_{\text{orb}}$. To represent the range of disk conditions, we sample fairly in time with $\Delta t = 0.1t_{\text{osc}}$ for a period $2t_{\text{osc}}$ starting from $1t_{\text{orb}}$.

For each LOS, H I 21 cm emission/absorption lines are constructed as follows. We first extract the LOS number density $n(s)$, temperature $T_k(s)$, and velocity $v(s)$ as a function of the path length s along a pencil beam at (l, b) . We hereafter omit the functional dependence on s for convenience. The local Cartesian coordinates (x, y, z) can be converted to the Galactic coordinates (s, l, b) using

$$\begin{aligned} x &= -s \cos b \cos l \\ y &= -s \cos b \sin l \\ z &= s \sin b. \end{aligned}$$

Along each ray, we sample at an interval of $\Delta s = 2$ pc, calculating the physical quantities via a trilinear interpolation with the eight nearest grid zones. The background rotational velocity relative to the observer $\mathbf{v}_0 = (0, -\Omega x, 0)$ is also added to the LOS velocity. The path length is increased until the vertical coordinate z reaches the boundary of the simulation, $z = \pm L_z/2$, by making use of the periodic boundary conditions in the horizontal direction. Since our numerical model is local, it is unphysical to perform mock observations toward very low b , for which the path length would extend beyond the disk scale length $R_d \sim 3.75$ kpc (Kalberla & Kerp 2009). For this reason, we limit the path length to be smaller than $s_{\text{max}} = 3$ kpc, resulting in a minimum latitude for LOSs of $b_{\text{min}} = 4.9^\circ$.

In order to illustrate our virtual H I sky, we calculate the column density and the harmonic mean temperature as $N_{\text{H}} \equiv \int n ds$ and $T_{k,\text{avg}} \equiv N_{\text{H}} / \int (n/T_k) ds$, respectively. Figure 1 displays airtoff projection images of (a) N_{H} and (b) $T_{k,\text{avg}}$ at $t/t_{\text{orb}} = 1$. Here, for visualization purpose only, we evenly divide the Galactic longitude and latitude with 1° resolution down to $|b| = 0$, while mock observations used in this paper are randomly and fairly sampled within an unit solid angle as described above. Note again that the path length is artificially limited to $s_{\text{max}} = 3$ kpc for $|b| < 5^\circ$. The overall morphology of the column density map resembles the radio survey maps quite well (e.g., Kalberla et al. 2005).

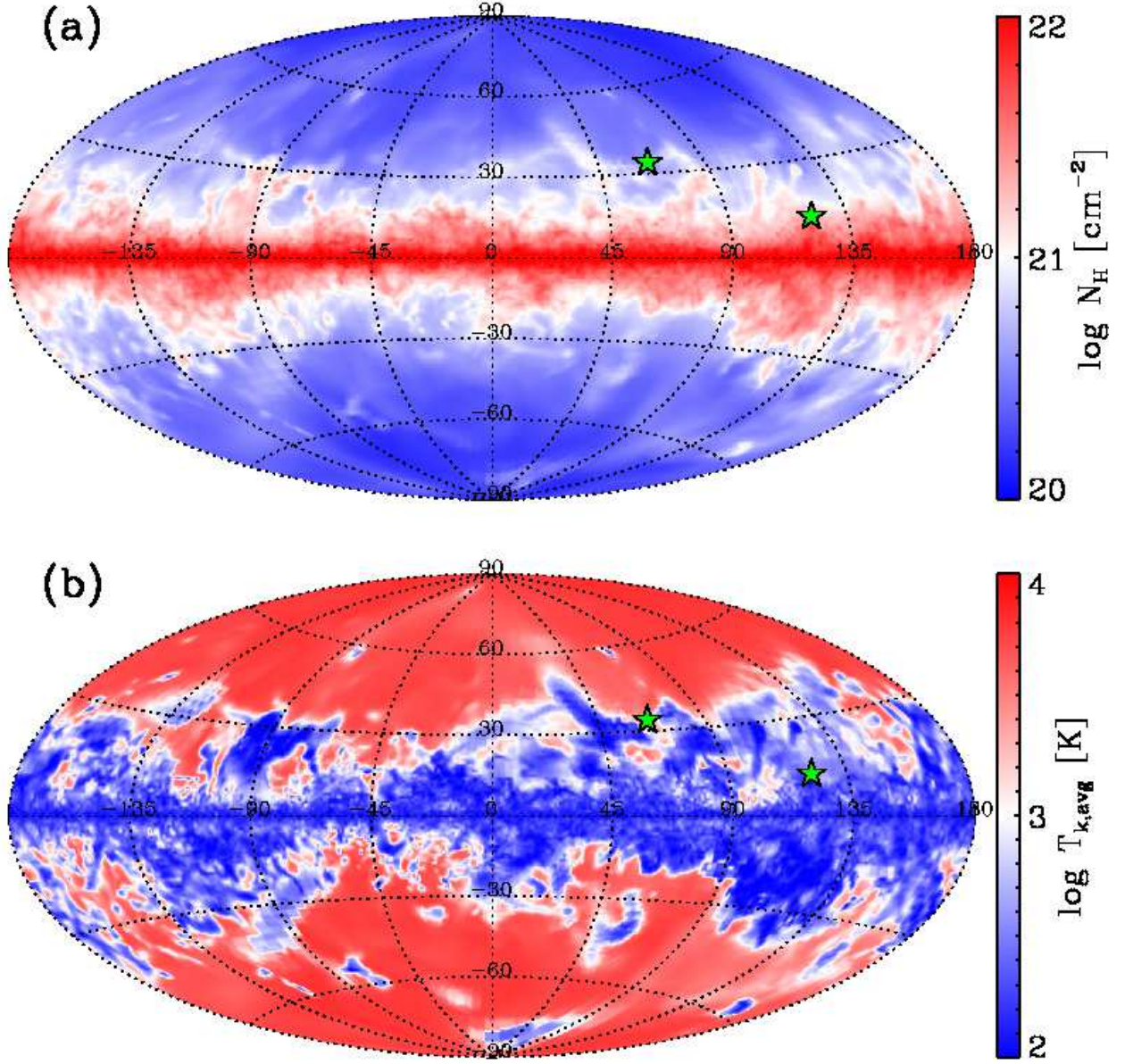


Fig. 1.— Aitoff projection maps of (a) column density (N_H) and (b) harmonic mean temperature ($T_{k,\text{avg}}$) at $t/t_{\text{orb}} = 1$. The locations of two sample LOSs presented in Figures 3 and 4 are marked with green stars in both panels.

2.3. Synthetic H I Lines

The emissivity and absorption coefficient² of the 21 cm line are respectively given by (e.g., Spitzer 1978; Draine 2011)

$$j(v_{\text{ch}}) = \frac{3}{16\pi} h\nu_0 A_{10} n \phi(v_{\text{ch}}) \quad (1)$$

and

$$\kappa(v_{\text{ch}}) = \frac{3}{32\pi} \frac{hc^2}{k\nu_0} A_{10} \frac{n}{T_s} \phi(v_{\text{ch}}), \quad (2)$$

where $\nu_0 = 1.4204$ GHz is the frequency at the line center, $A_{10} = 2.8843 \times 10^{-15} \text{ s}^{-1}$ is the Einstein A coefficient of the line (Gould 1994), and $\phi(v_{\text{ch}})$ is the normalized line profile as a function of velocity that satisfies $\int \phi(v_{\text{ch}}) \frac{\nu_0}{c} dv_{\text{ch}} = 1$. We assume a Gaussian velocity distribution

$$\phi(v_{\text{ch}}) = \frac{1}{\sqrt{\pi} \Delta v} \frac{c}{\nu_0} e^{-[(v_{\text{ch}} - v)/\Delta v]^2}, \quad (3)$$

where $\Delta v \equiv (2kT_k/m_H)^{1/2}$ is the Doppler width of the line. In order to calculate the absorption coefficient, we need the spin temperature, T_s , at each point along the LOS.

The spin temperature is defined such that the Boltzmann distribution at T_s gives the actual level populations. There are three principal mechanisms that determine the level populations of the hyperfine state: collisional transitions, direct radiative transitions by 21 cm photons, and indirect radiative transitions involving intermediate levels mainly by scattered Ly- α photons (the Wouthuyen-Field (WF) effect; Wouthuysen 1952; Field 1958). Including all three processes and assuming a balance between excitation and de-excitation, we can calculate the actual level population. The spin temperature is then given by a weighted mean of gas kinetic temperature T_k , the brightness temperature of the background 21 cm radiation field $T_R = 3.77 \text{ K}^3$, and the effective temperature of the Ly- α field T_α (Field 1958, see also Liszt 2001):

$$T_s = \frac{T_R + y_c T_k + y_\alpha T_\alpha}{1 + y_c + y_\alpha}, \quad (4)$$

where the normalized transition probabilities via collisions and Ly- α photons are respectively given by

$$y_c \equiv \frac{T_0}{T_k} \frac{R_{10}^c}{A_{10}} \quad \text{and} \quad y_\alpha \equiv \frac{T_0}{T_\alpha} \frac{R_{10}^\alpha}{A_{10}}. \quad (5)$$

Here, R_{10}^c and R_{10}^α are the rates of net downward transition by collision and the WF effect at given temperatures T_k and T_α , respectively, and $T_0 \equiv h\nu_0/k = 0.0681 \text{ K}$. If collisions dominate the

²Here, the emissivity is energy per unit volume per unit time per unit solid angle, and we use symbol κ not for the opacity (the absorption cross section per mass), but for the absorption cross section per unit volume.

³This includes the cosmic microwave background and Galactic synchrotron emission near the 21 cm line (Draine 2011, Chapter 17).

transition between levels, $T_s = T_k$. However, for typical conditions in the WNM, T_s departs from T_k since the rate of collisional transitions is insufficient for “thermalization” (Liszt 2001).

We assume that neutral hydrogen is the only collisional partner and adopt an approximate expression for the collisional de-excitation rate coefficient (Draine 2011, Chapter 17; see also Allison & Dalgarno 1969; Zygelman 2005; Furlanetto et al. 2006)

$$k_{10} \approx \begin{cases} 1.19 \times 10^{-10} T_2^{0.74-0.20 \ln T_2} \text{ cm}^{-3} \text{ s}^{-1} & 20 \text{ K} < T_k < 300 \text{ K} \\ 2.24 \times 10^{-10} T_2^{0.207} e^{-0.876/T_2} \text{ cm}^{-3} \text{ s}^{-1} & 300 \text{ K} < T_k < 10^3 \text{ K} \end{cases}, \quad (6)$$

where $T_2 = T_k/100 \text{ K}$. For $T_k > 10^3 \text{ K}$, we extrapolate the second expression for k_{10} . Collisional de-excitation due to electron impact is less than that from neutral hydrogens provided the ionization fraction remains less than 3%, which is generally the case for the CNM and WNM in the solar neighborhood (Wolfire et al. 1995). The net downward transition rate is $R_{10}^c = nk_{10}$.

We consider the WF effect using the simple parameterized formula for y_α derived by Field (1958):

$$y_\alpha = 5.9 \times 10^{11} \frac{n_\alpha}{T_\alpha T_k^{1/2}}, \quad (7)$$

where n_α is the Ly- α photon number density near the Ly- α line center. T_α is determined by the spectrum near Ly- α , which involves a difficult scattering problem. To a first approximation, Wouthuysen (1952) and Field (1958) argued that the spectrum near Ly- α is given by the Planck curve corresponding to the atomic kinetic temperature so that $T_\alpha = T_k$ (see also Field 1959).⁴ We adopt a fixed value of $n_\alpha = 10^{-6} \text{ cm}^{-3}$ for galactic Ly- α radiation (c.f., Liszt 2001).

Since we simply adopt a single, somewhat large value for n_α , the current treatment gives an upper limit of the WF effect (although the WF effect is still insufficient to fully thermalize the WNM – cf. Liszt 2001). For a lower limit on the WNM spin temperature, we use the spin temperature neglecting the WF effect. Note that the WF effect has little impact for the overall results in this paper in spite of about an order of magnitude difference in the spin temperature of the WNM. This is because we consider channel- or LOS-integrated properties, which are dominated not by the low-optical depth WNM but by the high- or intermediate-optical depth gas. In the remainder of this paper, we mainly present results based calculations of T_s without the WF effect (where we have found it is unimportant), while we compare results with and without the WF effect when it produces any non-negligible differences.

Figure 2 displays the distribution of the spin temperature T_s without the WF effect (*top row*; (a) and (b)) and with the WF effect (*bottom row*; (c) and (d)) as a function of the kinetic

⁴If there are significant non-thermal motions of gas with one-dimensional velocity dispersion of v_{turb} , the Doppler temperature, $T_D \equiv T_k + m_H v_{\text{turb}}^2/k$, should be considered instead of the kinetic temperature (Liszt 2001; Draine 2011). Since we already rely on specific (uncertain) parameter n_α to include the WF effect, however, we limit ourselves to the simplest approximation; we note that the turbulent velocity dispersion on large scales in our simulations does not exceed the warm-medium thermal velocity dispersion.

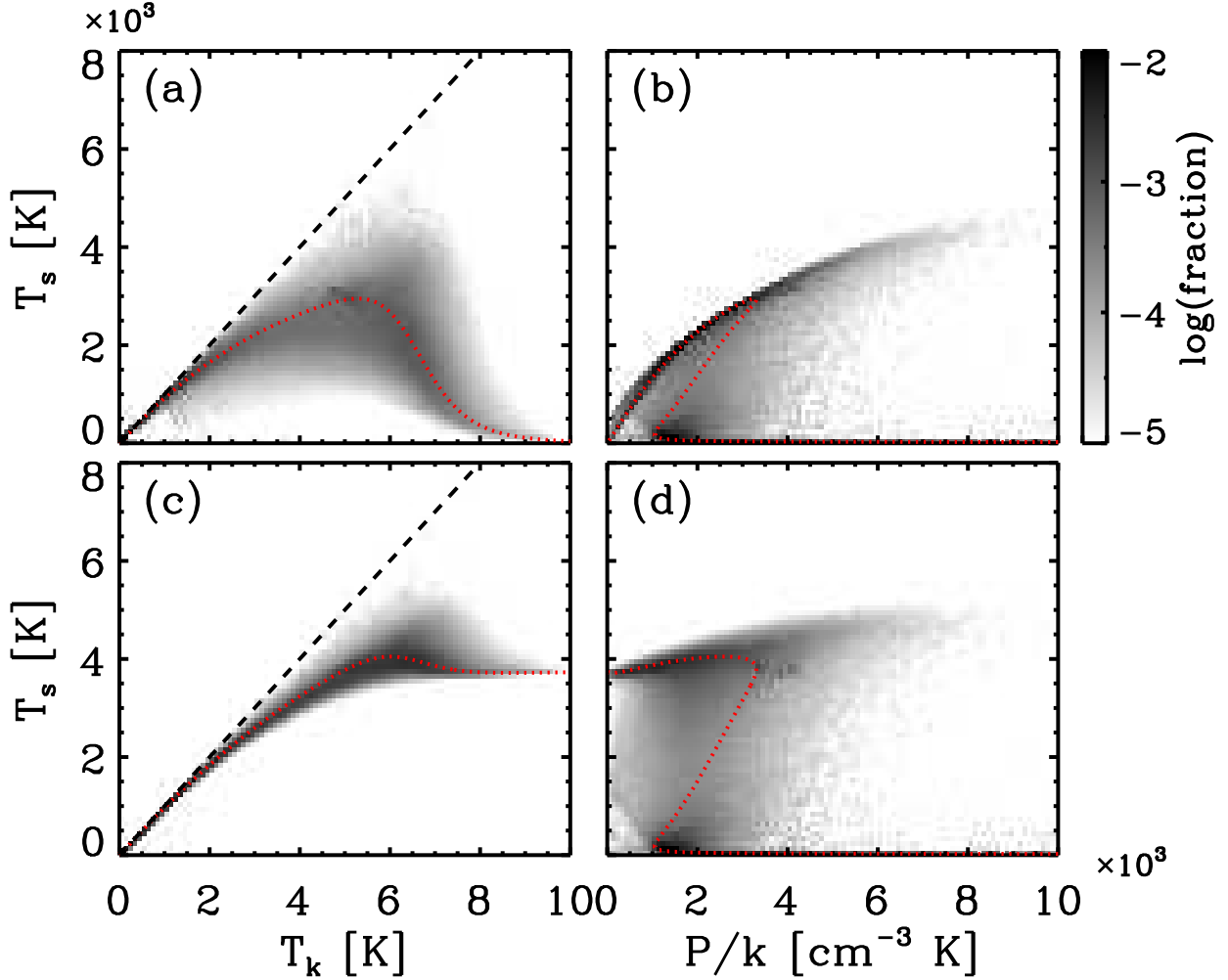


Fig. 2.— Distribution of the spin temperature T_s without (*top row*) and with (*bottom row*) the WF effect as a function of the kinetic temperature T_k (*left column*) the thermal pressure P/k (*right column*) for model QA10 at $t/t_{\text{orb}} = 1$. The grey scale displays the logarithmic fraction of the total mass for all simulated LOSs in each bin. The black dashed line in (a) and (c) stands for $T_s = T_k$. The red dotted line denotes the spin temperature taking density equal to the thermal equilibrium value, $n_{\text{eq}} = \Gamma/\Lambda(T_k)$, at a given T_k . At $T_k > 5000$ K, the equilibrium spin temperature drops (strongly without WF in (a), slightly with WF in (c)). Panels (b) and (d) show that this corresponds to low-pressure gas with $P/k < 10^3 \text{ cm}^{-3} \text{ K}$, away from the midplane in the simulation. Out-of-equilibrium gas is also evident for $T_k > 1000$ K.

temperature T_k (*left column*; (a) and (c)) and the thermal pressure $P/k = 1.1nT_k$ (*right column*; (b) and (d)) for the snapshot at $t/t_{\text{orb}} = 1$ of the QA10 model. The grey scale represents the fraction of the total mass in each bin. The red dotted line denotes the value of the spin temperature calculated along the thermal equilibrium density curve, $n_{\text{eq}} \equiv \Gamma/\Lambda(T_k)$, for the average heating rate of the QA10 model $\Gamma = 1.6 \times 10^{-26} \text{ erg s}^{-1}$ and using Λ given by Equation (6) of Paper I.

Figure 2 shows that $T_s \sim T_k$ for the gas at $T_k < 500 \text{ K}$, whereas a range of T_s is possible for the warm and unstable gas with $T_k > 1000 \text{ K}$. Note however that low values of T_s in warm gas (without the WF effect) occur only when the pressure is quite low, far from the midplane. The WF effect brings T_s closer to T_k at low density and pressure (panels (c) and (d)), but the transition is still not thermalized. Since most of the gas is close to thermal equilibrium (because the cooling time is shorter than the dynamical time), the most populated part of the distribution follows the equilibrium curve. However, a non-negligible fraction of gas is out-of-equilibrium with higher/lower density than n_{eq} due to dynamical contraction/expansion, resulting in higher/lower spin temperature than the red dotted line (see also Figures 8 and 10 of Paper I). In practice, without the WF effect, the density range for out-of-equilibrium gas is quite wide (more than an order of magnitude) so that T_s spans from a few hundreds of Kelvin to T_k when $T_k > 1000 \text{ K}$. With the WF effect, T_s of the WNM is generally larger than 1000 K but still significantly smaller than T_k .

Given T_s , we now can calculate the absorption coefficient from Equation (2), and the contribution to the local optical depth from the i -th element along a LOS is then $\tau^i(v_{\text{ch}}) = \kappa(v_{\text{ch}}; s_i)\Delta s$, where $s_i = i\Delta s$. The total optical depth along a LOS for a given velocity channel v_{ch} is then:

$$\tau(v_{\text{ch}}) = \sum_{i=1}^N \tau^i(v_{\text{ch}}), \quad (8)$$

where N is the total number of LOS elements in a given (l, b) direction. The synthetic emission line is constructed by summing up the brightness temperature of each element with foreground attenuation:

$$T_B(v_{\text{ch}}) = \sum_{i=1}^N \left[T_s^i (1 - e^{-\tau^i(v_{\text{ch}})}) \exp \left(- \sum_{j=1}^{i-1} \tau^j(v_{\text{ch}}) \right) \right]. \quad (9)$$

We use velocity channels with resolution $\Delta v_{\text{ch}} = 1 \text{ km s}^{-1}$ from -50 km s^{-1} to 50 km s^{-1} .

Figures 3 and 4 plot examples of high and low optical depth LOSs toward $(l, b) = (121^\circ, 12^\circ)$ and $(l, b) = (66^\circ, 33^\circ)$ at $t/t_{\text{orb}} = 1$, respectively. In the *left column*, we plot (*top to bottom*) the number density, temperature, and velocity versus path length along the LOS. In the *right column*, we plot the synthetic emission ($T_B(v_{\text{ch}})$) and absorption ($1 - e^{-\tau(v_{\text{ch}})}$) lines as well as the “observed” spin temperature $T_{s,\text{obs}}(v_{\text{ch}})$ (see Equation (12)) as a function of velocity channel. The spin temperature T_s without the WF effect at each point along the LOS, and the harmonic mean spin temperature in each velocity channel, $T_{s,\text{avg}}(v_{\text{ch}})$ (see Equation (11)), are presented as red dotted lines in *middle-left* and *bottom-right* plots, respectively, while the blue dashed lines denote profiles with the WF effect. Note that the optical depth is slightly decreased due to the WF effect

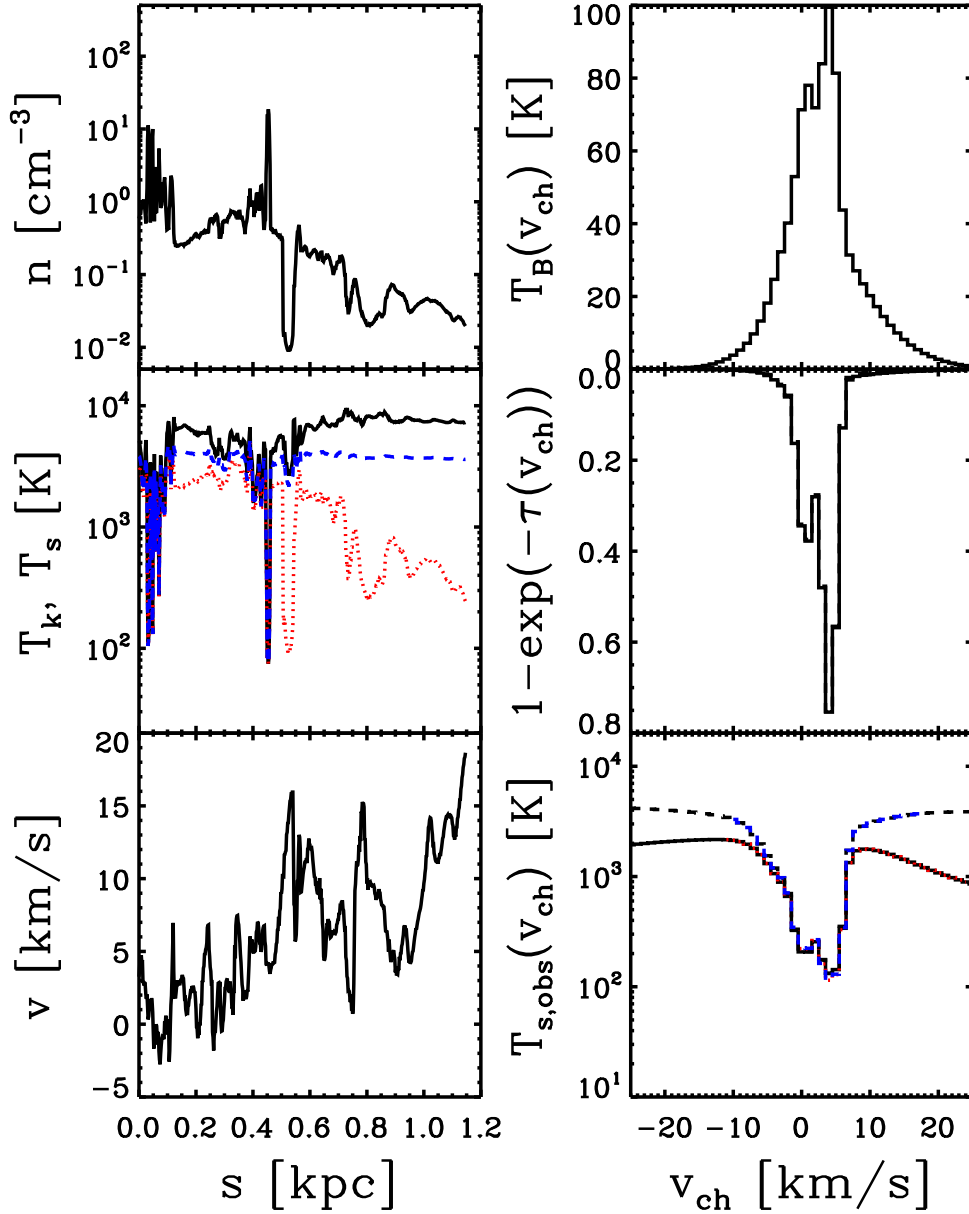


Fig. 3.— Example LOS toward direction with high- τ , $(l, b) = (121^\circ, 12^\circ)$ at $t/t_{\text{orb}} = 1$. *Left*: From *top* to *bottom*, we plot in black the number density n , temperature T_k , and velocity v as functions of the path length s along the LOS. In the *middle* plot, the spin temperature T_s is shown with (blue dashed) and without (red dotted) the WF effect. Without WF, T_s drops at large distance from the midplane where the pressure is low. *Right*: From *top* to *bottom*, we plot the brightness temperature $T_B(v_{\text{ch}})$ (synthetic emission line), the optical depth $1 - e^{-\tau(v_{\text{ch}})}$ (synthetic absorption line), and the “observed” spin temperature $T_{s,\text{obs}}(v_{\text{ch}}) \equiv T_B(v_{\text{ch}})/(1 - e^{-\tau(v_{\text{ch}})})$ as functions of velocity channel. In the *middle* and *bottom* plots, solid black lines are without and dashed lines are with the WF effect. Note that solid and dashed lines in the *middle* plot are indistinguishable for high- τ channels (see Figure 4 for low- τ channels). In the *bottom* plot, the harmonic mean spin temperature $T_{s,\text{avg}}(v_{\text{ch}})$ defined by Equation (11) is shown with (blue dashed) and without (red dotted) the WF effect. The “observed” spin temperature agrees with the “true” harmonic mean spin temperature either with or without the WF effect. See Section 3.1 for details.

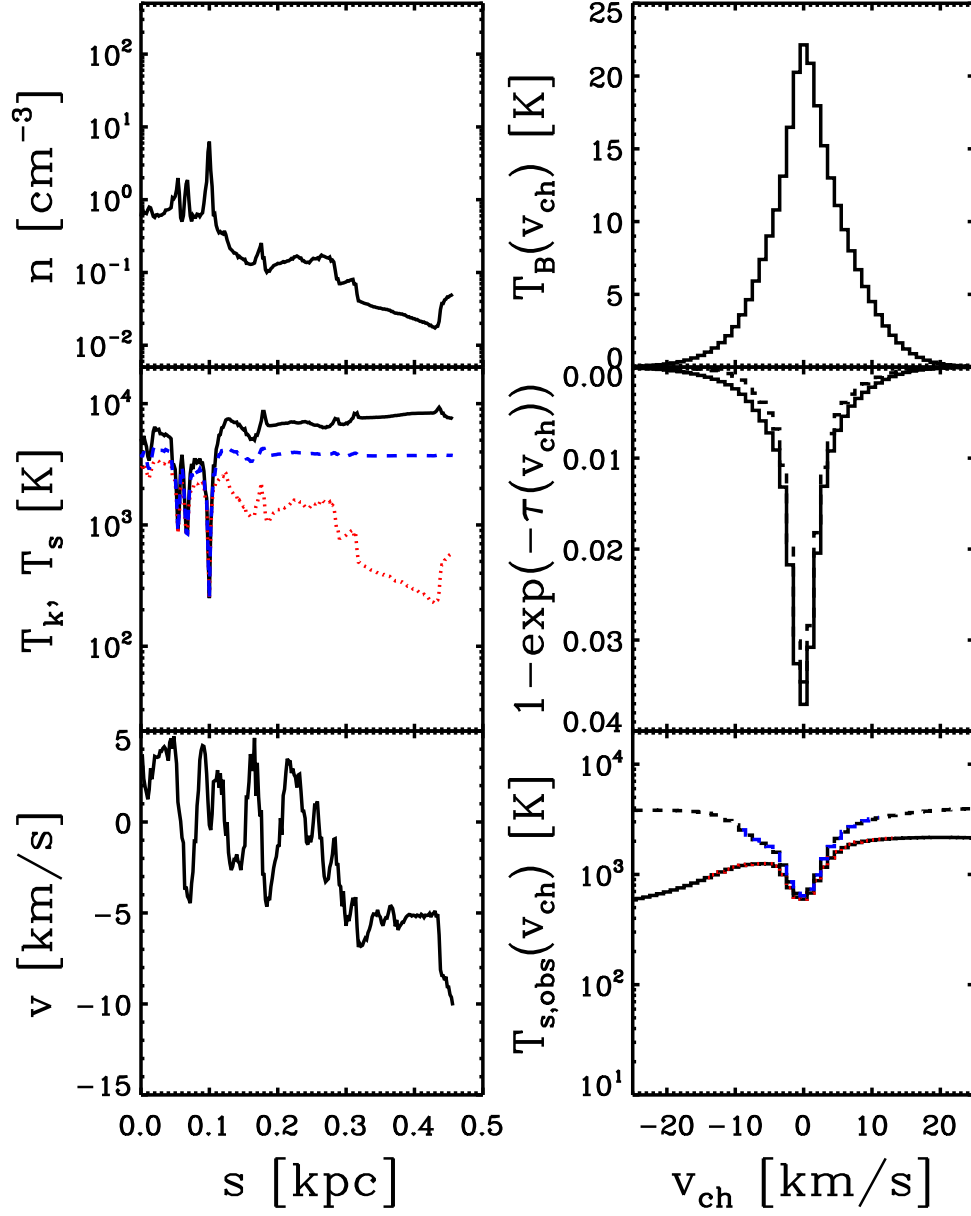


Fig. 4.— Same as Figure 3 but for low- τ LOS, $(l, b) = (66^\circ, 33^\circ)$.

(dashed line in *middle-right* plot), while the synthetic emission remains unchanged. We only plot $T_{s,\text{avg}}(v_{\text{ch}})$ for $\tau(v_{\text{ch}}) > 10^{-3}$ to show the range of synthetic lines we use for further analysis. From Figure 3, it is evident that density structure is quite complicated along a given LOS, even when $T_B(v_{\text{ch}})$ and $\tau(v_{\text{ch}})$ are relatively simple.

3. Extraction of Physical Properties from Synthetic Lines

3.1. Column Density and Spin Temperature

The column density and harmonic mean spin temperature are the main physical properties that can be inferred directly from the H I 21 cm emission and absorption lines observations (e.g., Heiles & Troland 2003b; Kalberla et al. 2005; Dickey et al. 2009). From Equations (2) and (8), integrating the density along the LOS gives

$$N_{\text{H}} = \int n ds = 1.813 \times 10^{18} \text{ cm}^{-2} \int T_{s,\text{avg}}(v_{\text{ch}}) \tau(v_{\text{ch}}) dv_{\text{ch}} \quad (dv_{\text{ch}} \text{ in km s}^{-1}), \quad (10)$$

where the harmonic mean spin temperature for a given velocity channel is defined by

$$T_{s,\text{avg}}(v_{\text{ch}}) \equiv \frac{\int \kappa(v_{\text{ch}}) T_s ds}{\tau(v_{\text{ch}})} = \frac{\int \kappa(v_{\text{ch}}) T_s ds}{\int \kappa(v_{\text{ch}}) ds} = \frac{\int n \phi(v_{\text{ch}}) ds}{\int (n/T_s) \phi(v_{\text{ch}}) ds}. \quad (11)$$

Note, however, that $T_{s,\text{avg}}(v_{\text{ch}})$ is not a direct observable since the definition in Equation (11) requires full LOS information. For observations, an “observed” spin temperature in a given velocity channel is defined by

$$T_{s,\text{obs}}(v_{\text{ch}}) \equiv \frac{T_B(v_{\text{ch}})}{1 - e^{-\tau(v_{\text{ch}})}}, \quad (12)$$

where $T_B(v_{\text{ch}})$ is the observed brightness temperature, and $1 - e^{-\tau(v_{\text{ch}})}$ is obtained by differencing off and on a background source. By inspecting Equation (9), the approximation $T_{s,\text{obs}}(v_{\text{ch}}) \approx T_{s,\text{avg}}(v_{\text{ch}})$ holds for channels with low optical depth and absorption dominated by a single layer (Spitzer 1978). By comparing $T_{s,\text{avg}}(v_{\text{ch}})$ (red and blue) and $T_{s,\text{obs}}(v_{\text{ch}})$ (black solid and dashed) in *bottom-right* panels of Figures 3 and 4, we can see that the “observed” spin temperatures inferred from the lines in fact agree quite well with the corresponding harmonic mean spin temperatures even near the line center with large optical depth. This is true whether or not WF effect contributes to setting the spin temperature.

In order to quantify the agreement between the “observed” and “true” harmonic-mean spin temperatures, we calculate $T_{s,\text{obs}}(v_{\text{ch}})/T_{s,\text{avg}}(v_{\text{ch}})$ as a function of the channel optical depth $\tau(v_{\text{ch}})$ for all LOSs and channels of a snapshot at $t/t_{\text{orb}} = 1$. Figure 5 displays the distribution for the case without WF in grey scale. As expected, if the channel is optically thin $\tau(v_{\text{ch}}) \lesssim 0.1$, the two spin temperatures are in very good agreement. The difference emerges at $\tau(v_{\text{ch}}) \gtrsim 0.1$ and gets larger as the channel optical depth increases. $T_{s,\text{obs}}(v_{\text{ch}})$ can either under- or overestimate the “true” harmonic mean spin temperature, but remains within a factor of 1.2 and 1.5 of $T_{s,\text{avg}}(v_{\text{ch}})$

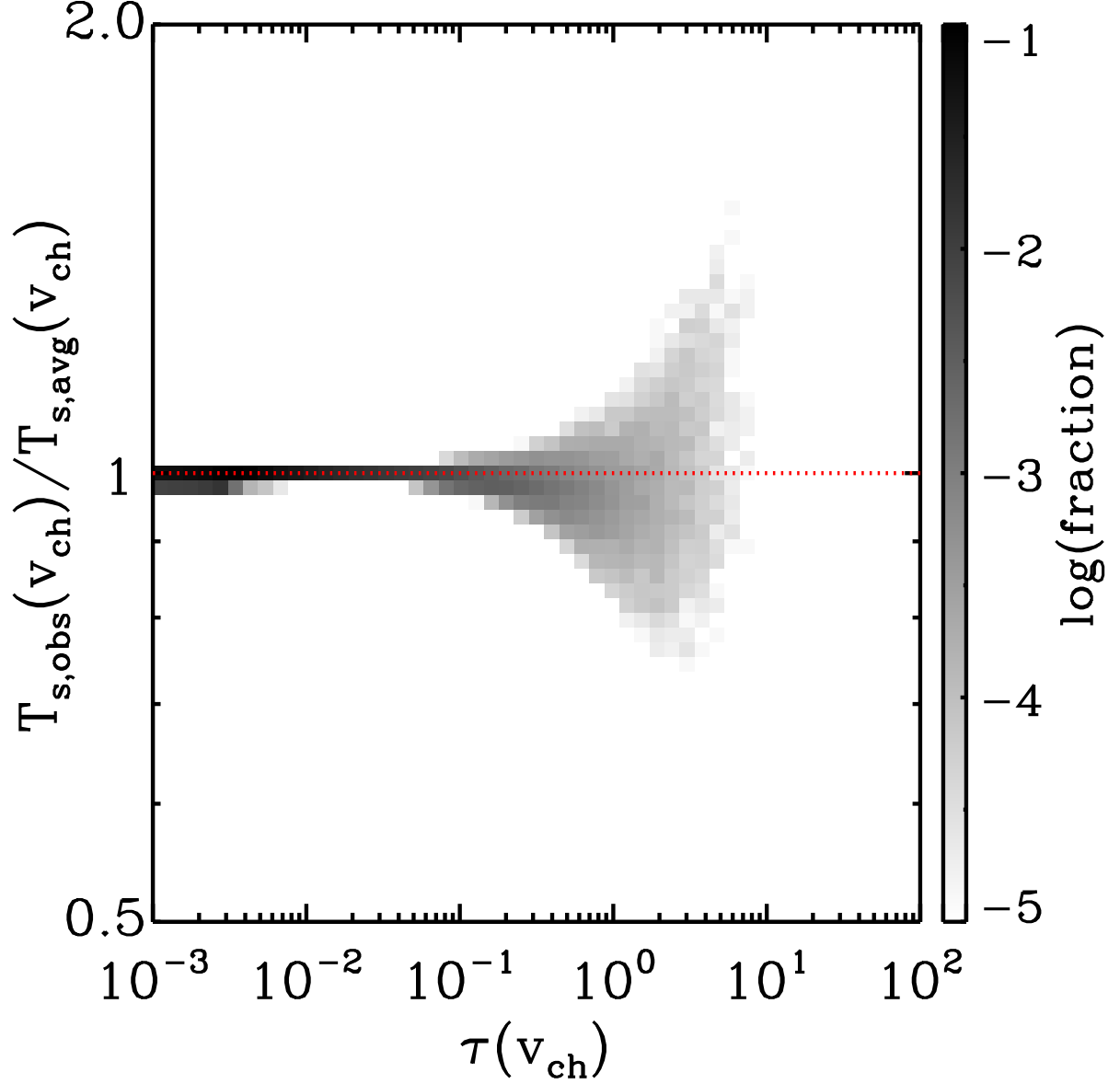


Fig. 5.— Distribution of the ratio of the “observed” to “true” spin temperatures $T_{s,obs}(v_{ch})/T_{s,avg}(v_{ch})$ as a function of the channel optical depth $\tau(v_{ch})$ for all LOSs and channels at $t/t_{orb} = 1$. The grey scale displays the fraction of the whole distribution in each bin. With the WF effect, this distribution remains unchanged.

for the channel optical depth of $\tau(v_{\text{ch}}) \sim 1$ and 10, respectively. Note that T_s is larger when the WF effect is included, which reduces both the contribution to the harmonic-mean average spin temperature and the contribution to the optical depth, from warm regions in each velocity channel. The agreement between $T_{s,\text{obs}}(v_{\text{ch}})$ and $T_{s,\text{avg}}(v_{\text{ch}})$ is best at low optical depth, so the use of lower limit for the WNM spin temperature (omitting WF) provides a conservative conclusion for the agreement between “observed” and “true” values. We have also directly checked that when the WF effect is included, Figure 5 is essentially unchanged.

We now explore using $T_{s,\text{obs}}(v_{\text{ch}})$ as a proxy for $T_{s,\text{avg}}(v_{\text{ch}})$ to obtain the “observed” column density from the synthetic lines. Substituting Equation (12) for $T_{s,\text{avg}}(v_{\text{ch}})$ in Equation (10),

$$N_{\text{H,obs}} \equiv 1.813 \times 10^{18} \text{ cm}^{-2} \int \frac{\tau(v_{\text{ch}})T_B(v_{\text{ch}})}{1 - e^{-\tau(v_{\text{ch}})}} dv_{\text{ch}} \quad (dv_{\text{ch}} \text{ in km s}^{-1}). \quad (13)$$

The quantities on the right-hand side are all observables; Equation (13) is also known as the “isothermal” estimator of the H I column density (Spitzer 1978; Dickey & Benson 1982; Chengalur et al. 2013). In the optically-thin limit, we have the “thin” column density

$$N_{\text{H,thin}} \equiv 1.813 \times 10^{18} \text{ cm}^{-2} \int T_B(v_{\text{ch}}) dv_{\text{ch}} \quad (dv_{\text{ch}} \text{ in km s}^{-1}), \quad (14)$$

which is what observers obtain when there is no absorption line information. The “observed” spin temperature obtained from an optical-depth weighted average in a given LOS is:

$$T_{s,\text{obs}} \equiv \frac{\int \tau(v_{\text{ch}})T_{s,\text{obs}}(v_{\text{ch}}) dv_{\text{ch}}}{\int \tau(v_{\text{ch}}) dv_{\text{ch}}}. \quad (15)$$

Figure 6 displays distributions of the mock observational data for the ratios of “observed” to “true” (a) column density $N_{\text{H,obs}}/N_{\text{H}}$ and (b) harmonic mean spin temperature $T_{s,\text{obs}}/T_{s,\text{avg}}$ as a function of the integrated optical depth $\tau_{\text{int}} \equiv \int \tau(v_{\text{ch}}) dv_{\text{ch}}$. Figure 6 includes all LOSs and all temporal snapshots over an interval $2t_{\text{osc}}$ (rather than a single data dump) from the simulation. Here, the “true” harmonic mean spin temperature is defined by $T_{s,\text{avg}} \equiv \int nds / \int (n/T_s) ds$, which can also be obtained by taking the optical depth weighted average of $T_{s,\text{avg}}(v_{\text{ch}})$ analogous to Equation (15). Since $T_{s,\text{obs}}(v_{\text{ch}})$ reproduces $T_{s,\text{avg}}(v_{\text{ch}})$ very well, $N_{\text{H,obs}}$ and $T_{s,\text{obs}}$ also give excellent estimates of the true column density and harmonic mean spin temperature, respectively. In particular, 90% and 99% of all LOSs respectively have $N_{\text{H,obs}}$ and $T_{s,\text{obs}}$ within 5% and 12% of the true values. As in Figure 6, the estimators are best at low τ_{int} . The bulk of underestimated data points shown near $\tau_{\text{int}} \sim 0.5$ are due to a specific snapshot at $t/t_{\text{orb}} = 1.3$, when a cold cloud happens to surround the virtual observer. The cold cloud surrounding the observer provides foreground absorption at moderate opacity for all LOSs, violating the assumption of a single cold layer and resulting in overall underestimation of $T_{s,\text{obs}}(v_{\text{ch}})$ and hence $N_{\text{H,obs}}$ and $T_{s,\text{obs}}$.

The distribution of the ratio of the “thin” (Equation 14) to “true” column density is shown as thin contours in Figure 6(a). Evidently, $N_{\text{H,thin}}$ significantly underestimates the “true” column density when $\tau_{\text{int}} > 1$. However, the majority of the $N_{\text{H,thin}}/N_{\text{H}}$ distribution remains > 0.7 up

to $\tau_{\text{int}} < 10$, while the distribution extends to values as small as ~ 0.2 at high τ_{int} . In observations, $N_{\text{H,thin}}/N_{\text{H,obs}} \sim 0.6 - 0.8$ for $N_{\text{H,obs}} \sim 4 - 20 \times 10^{21} \text{ cm}^{-2}$ (Dickey et al. 2003, see also Dickey & Benson 1982).

3.2. CNM MASS FRACTION

Another important physical property that can be deduced from emission/absorption line observations is the CNM mass fraction (e.g., Dickey et al. 2009). In the classical two phase picture of the ISM (e.g., Field et al. 1969; Wolfire et al. 1995), the harmonic mean kinetic temperature $T_{k,\text{avg}}$ along the LOS is defined by

$$\frac{N_{\text{H}}}{T_{k,\text{avg}}} \equiv \frac{N_{\text{c}}}{T_{\text{c}}} + \frac{N_{\text{w}}}{T_{\text{w}}}, \quad (16)$$

where N_{c} and N_{w} are the column density of the CNM and WNM, respectively, and T_{c} and T_{w} are the temperature of the CNM and WNM, respectively. Since $T_{\text{c}} \ll T_{\text{w}}$, the CNM mass fraction $f_{\text{c}} \equiv N_{\text{c}}/N_{\text{H}} \approx T_{\text{c}}/T_{k,\text{avg}}$ unless f_{c} is extremely small.

Similarly, for a two phase ISM, Equation (15) can be simplified (using Equation (10) and $T_{s,\text{obs}}(v_{\text{ch}}) \approx T_{s,\text{avg}}(v_{\text{ch}})$) as

$$\frac{N_{\text{H,obs}}}{T_{s,\text{obs}}} \approx \frac{N_{\text{c}}}{T_{s,c}} + \frac{N_{\text{w}}}{T_{s,w}} \approx \frac{N_{\text{c}}}{T_{\text{c}}} + \frac{N_{\text{w}}}{T_{s,w}}, \quad (17)$$

where $T_{s,c}$ and $T_{s,w}$ are the spin temperatures of the CNM and WNM, respectively. The second approximation in Equation (17) utilizes $T_{s,c} \approx T_{\text{c}}$ from Figure 2. This gives

$$f_{c,\text{obs}} \equiv \frac{N_{\text{c}}}{N_{\text{H,obs}}} = \frac{T_{\text{c}}}{T_{s,\text{obs}}} \left(\frac{T_{s,w} - T_{s,\text{obs}}}{T_{s,w} - T_{\text{c}}} \right). \quad (18)$$

Here, we have used $N_{\text{H,obs}} \approx N_{\text{H}}$ and we keep the term in parentheses since typical spin temperatures of the WNM are not as high as the kinetic temperature of the WNM (see Figure 2). Thus, for a given $T_{s,\text{obs}}$, one can estimate the CNM mass fraction by assuming a value of T_{c} and $T_{s,w}$. If $T_{s,w} \gg T_{s,\text{obs}}$, then $f_{c,\text{obs}} \sim T_{\text{c}}/T_{s,\text{obs}}$.

In order to test the feasibility of this method, we first calculate the “true” mass fractions of the CNM (f_{c} ; $T_{\text{k}} < 184 \text{ K}$), unstable neutral medium (UNM, f_{u} ; $184 \text{ K} < T_{\text{k}} < 5050 \text{ K}$), and WNM (f_{w} ; $T_{\text{k}} > 5050 \text{ K}$) for a given LOS by integrating number density n of each component directly. Figure 7 plots the distribution of the “true” mass fractions of (a) CNM (b) UNM and (c) WNM as a function of the “observed” spin temperature $T_{s,\text{obs}}$ without the WF effect for all LOSs and snapshots. For $T_{s,\text{obs}} < 400 \text{ K}$, the main distribution of f_{c} follows roughly $f_{c,\text{obs}} \approx 80 \text{ K}/T_{s,\text{obs}}$, the “observed” CNM mass fraction. Here, we adopt $T_{\text{c}} = 80 \text{ K}$ based on the mean temperature of the CNM in the simulation. The scatter of the distribution indicates that the temperature of the CNM is not a constant but spans a range of $50 \text{ K} < T_{\text{c}} < 100 \text{ K}$ (see the dotted lines in Figure 7(a)). For $f_{\text{c}} < 0.2$ with $T_{s,\text{obs}} > 400 \text{ K}$, however, this simple approximation for f_{c} employing T_{c} alone is

Table 1. Model Parameters and Outcomes

Model (1)	Σ (2)	$\log \Sigma_{\text{SFR}}$ (3)	$\log P_{\text{th}}/k_{\text{B}}$ (4)	H_w (5)	N_{WNM} (6)
QA02	2.5	-4.11 ± 0.32	2.23 ± 0.16	347 ± 126	0.33
QA05	5	-3.43 ± 0.27	2.70 ± 0.15	202 ± 50	0.56
QA10	10	-2.82 ± 0.12	3.23 ± 0.10	111 ± 14	1.0
QA20	20	-2.18 ± 0.06	3.79 ± 0.04	59 ± 5	2.0

Note. — Column(1): model name from Paper I. Column (2): gas surface density ($\text{M}_{\odot} \text{ pc}^{-2}$). Column (3): logarithm of the SFR surface density ($\text{M}_{\odot} \text{ kpc}^{-2} \text{ yr}^{-1}$). Column (4): logarithm of the midplane thermal pressure ($\text{cm}^{-3} \text{ K}$). Column (5): scale height of the WNM (pc). Column (6): fiducial WNM-only vertical column density (see Equation (21); 10^{20} cm^{-2}). Columns (3)-(5) are averaged over $t/t_{\text{orb}} = 1 - 2$.

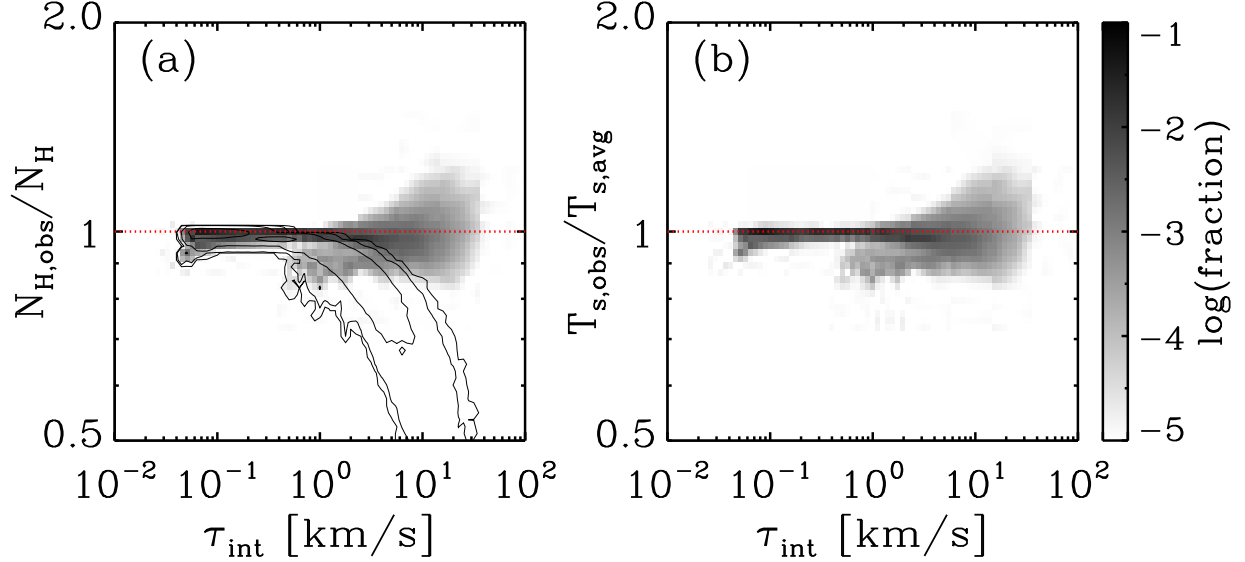


Fig. 6.— Distribution (grey scale) of the mock observation data of the ratios of “observed” to “true” (a) column density $N_{\text{H,obs}}/N_{\text{H}}$ and (b) harmonic mean spin temperature $T_{s,\text{obs}}/T_{s,\text{avg}}$ as a function of the integrated optical depth $\tau_{\text{int}} \equiv \int \tau(v_{\text{ch}}) dv_{\text{ch}}$ for all LOSs and simulation snapshots. The thin contours show the distribution for the ratio of “thin” to “true” column density $N_{\text{H,thin}}/N_{\text{H}}$. The contour levels from outside to inside correspond to the number fractions of 10^{-5} , 10^{-4} , 10^{-3} , 10^{-2} . See Equations (13), (14), and (15) for definitions of $N_{\text{H,obs}}$, $N_{\text{H,thin}}$, and $T_{s,\text{obs}}$, respectively.

no longer valid. Instead, by adopting $T_{s,w} = 1500$ K (the typical spin temperature of the WNM without the WF effect – see Figure 2(a) and (b)), we find that $f_{c,\text{obs}}$ from Equation (18) follows the overall trend of the f_c distribution quite well (see the dashed line in Figure 7(a)). In any case, the intrinsic scatter of this mass fraction estimator is as high as a factor of 2.

Figure 7(b) and (c) show that there is no regime in which either the UNM or the WNM is individually predominant in any range of the spin temperature. For the range of $200 \text{ K} < T_{s,\text{obs}} < 1000 \text{ K}$, the UNM is in the majority, but the WNM mass fraction is nearly comparable. For the range of $T_{s,\text{obs}} > 1000 \text{ K}$, the WNM becomes the majority, but the UNM fraction is still not negligible. The most probable UNM mass fraction is 30-50% for $T_{s,\text{obs}} > 1000 \text{ K}$. This implies that any attempt to use the spin temperature to estimate relative UNM and WNM abundances would not be reliable. Observation of spin temperature in the regime $T_{s,\text{obs}} \gtrsim 1000 \text{ K}$ only implies that there is negligible CNM.

Figure 8 shows the same distributions of phases as a function of the “observed” spin temperature $T_{s,\text{obs}}$, but now with the WF effect included. The distributions of all gas components are unchanged at $T_{s,\text{obs}} < 1000 \text{ K}$, while f_u and f_w distributions are stretched toward higher $T_{s,\text{obs}}$ at $T_{s,\text{obs}} > 1000 \text{ K}$. When the WF effect is included, T_s spans a narrower range at $T_{s,\text{obs}} > 1000 \text{ K}$ (see Figure 2), and as a result $f_w \rightarrow 1$ sharply at around $T_{s,\text{obs}} \sim 4000 \text{ K}$. Note however that the value of T_s above 1000 K is quite uncertain, as it depends on poorly constrained parameters controlling the WF effect; the specific values of f_w shown here in that range should therefore be considered cautiously. Taken together, Figures 7 (T_s without WF) and 8 (T_s with WF) imply that the typical “observed” spin temperature of the WNM (including substantial amount of the UNM) would be in a range between $1000\text{-}5000 \text{ K}$, consistent with previous calculation by Liszt (2001).

4. Comparison with Observations

4.1. Brightness Temperature, Optical Depth, and Spin Temperature

Classically, H I emission/absorption line observations have reported a negative correlation between the peak optical depth τ_{peak} and the spin temperature at the peak $T_{s,\text{peak}}$ since Lazareff (1975) first noted this correlation. The typical slope between $\log T_{s,\text{peak}}$ and $\log \tau_{\text{peak}}$ is found to be -0.35 (e.g., Payne et al. 1983; Kulkarni & Heiles 1987). As noted by Heiles & Troland (2003b) (see also Braun & Walterbos 1992), however, not only $T_{s,\text{peak}}$ and τ_{peak} but also N_{H} and Δv_{FWHM} are mutually related as

$$N_{\text{H}} = 1.93 \times 10^{20} \text{ cm}^{-2} \tau_{\text{peak}} \left(\frac{T_{s,\text{peak}}}{100 \text{ K}} \right) \left(\frac{\Delta v_{\text{FWHM}}}{\text{km s}^{-1}} \right), \quad (19)$$

which can be obtained by integrating Equation (2) over the LOS. Here $\Delta v_{\text{FWHM}} = 2\sqrt{\ln(2)}\Delta v$ is the full width at half maximum of the line profile. The multivariate analysis performed by Heiles & Troland (2003b) concludes that neither the historical $\tau_{\text{peak}}\text{-}T_{s,\text{peak}}$ relationship nor the

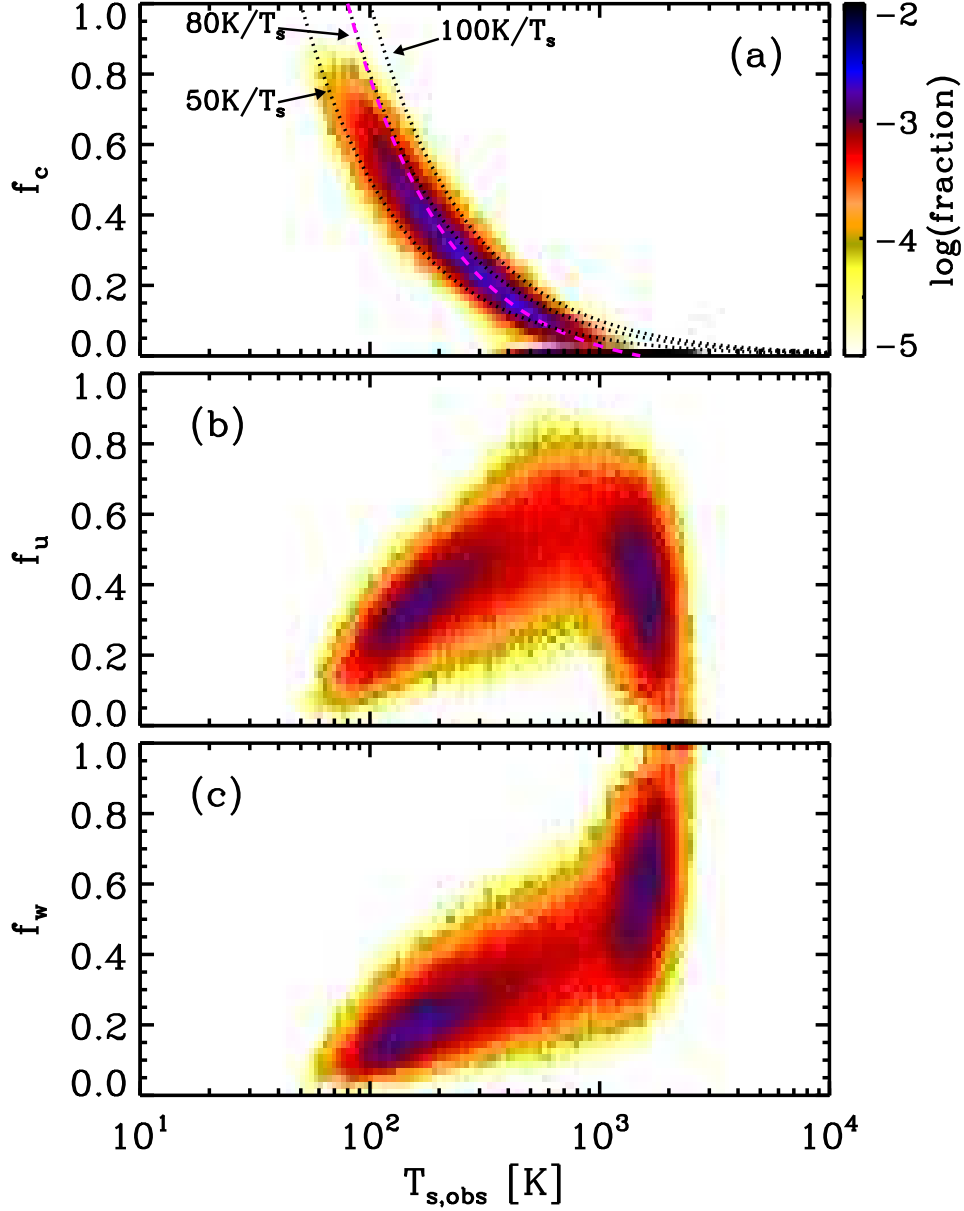


Fig. 7.— Distribution of the mass fractions of (a) cold (f_c ; $T_k < 184$ K), (b) thermally unstable (f_u ; $184 \text{ K} < T_k < 5050$ K), and (c) warm (f_w ; $T_k > 5050$ K) gas as a function of the “observed” mean spin temperature for all LOS and simulation snapshots. The black dotted lines in (a) denote $f_{c,\text{obs}} \approx T_c/T_{s,\text{obs}}$ for $T_c = 50$ K, 80 K, and 100 K from bottom to top. For $T_{s,\text{obs}} < 400$ K, the $T_c = 80$ K curve agrees well with f_c , and the $T_c = 50$ K and $T_c = 100$ K lines envelope the overall distribution. The magenta dashed line shows $f_{c,\text{obs}}$ (see Equation (18)) with $T_{s,w} = 1500$ K; this follows densest part of the distribution very well.

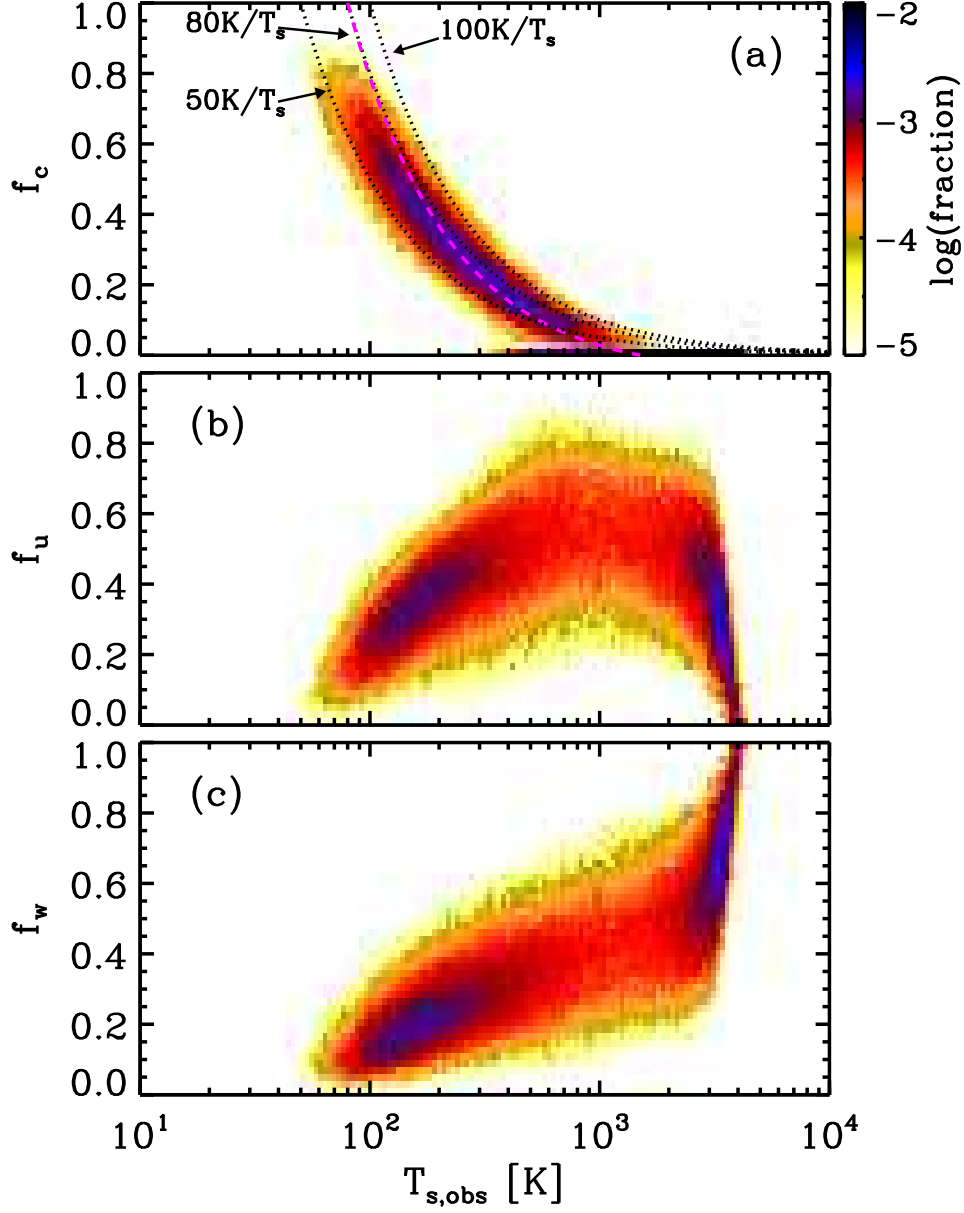


Fig. 8.— Same as Figure 7 but with the WF effect. Since T_s is larger with the WF effect for $T_k > 1000$ K and distributed in a narrower temperature range (see Figure 2), the WNM dominated region moves toward higher $T_{s,\text{obs}}$ with a sharp transition at around $T_{s,\text{obs}} = 4000$ K. Note that the distribution of f_c remains unchanged by the WF effect, and is well described by $f_{c,\text{obs}}$ with $T_{s,w} = 1500$ K (magenta dashed).

$\tau_{\text{peak}} N_{\text{H}} T_{s,\text{peak}}$ relationship has physical significance beyond the relation in Equation (19).

It is more informative to consider the distribution in three dimensional space of $T_B(v_{\text{ch}})$ - $\tau(v_{\text{ch}})$ - $T_{s,\text{obs}}(v_{\text{ch}})$ as in Figure 4 of Roy et al. (2013a). Figures 9 and 10 display distributions of the synthetic line data without and with the WF effect, respectively, in the plane of $T_B(v_{\text{ch}})$ and $\tau(v_{\text{ch}})$ for all LOSs, channels, and simulation snapshots of model QA10 with $dv_{\text{ch}} = 1 \text{ km s}^{-1}$. Different color contours in Figures 9(a) and 10(a) represent different spin temperature ranges: $T_{s,\text{obs}}(v_{\text{ch}}) < 200 \text{ K}$ in red, $200 \text{ K} < T_{s,\text{obs}}(v_{\text{ch}}) < 1000 \text{ K}$ in green, and $1000 \text{ K} < T_{s,\text{obs}}(v_{\text{ch}})$ in blue. Overlaid are the observational data points extracted from Figure 4 of Roy et al. (2013a). The distribution from our simulation follows the observed data points very well. Roy et al. (2013a) pointed out the lack of data points for low or intermediate optical depth measurements ($0.01 < \tau < 0.1$) in high ($T_B > 50 \text{ K}$; regime A) and intermediate ($1 \text{ K} < T_B < 10 \text{ K}$; regime B) brightness temperatures; these regions are also weakly populated by our synthetic line data.

To understand the paucity of data in the A regime, let us consider a LOS that consists only of static WNM. From Equation (19), we obtain $T_{s,\text{peak}} \tau_{\text{peak}} = 52 \text{ K} (N_{\text{H}}/10^{20} \text{ cm}^{-2}) (\Delta v_{\text{FWHM}}/\text{km s}^{-1})^{-1}$, and $N_{\text{H}} > 10^{21} \text{ cm}^{-2}$ is required for $\Delta v_{\text{FWHM}} = 10 \text{ km s}^{-1}$ to have $T_B \sim T_{s,\text{peak}} \tau_{\text{peak}} > 50 \text{ K}$. Since the WNM number density is about 0.3 cm^{-3} in the solar neighborhood (Wolfire et al. 1995), the path length would need to exceed 1 kpc to have $N_{\text{H}} > 10^{21} \text{ cm}^{-2}$. Note that this is lower limit since we assume a “static” medium. To have such a large column density for the WNM within a narrow velocity range, the path length would need to be much longer. It is thus highly unlikely to have no CNM along such a long path, which would be traversing a low- $|b|$ part of the ISM. Thus, for solar neighborhood conditions, the brightness temperature in a given channel would be as high as in regime A only if there are CNM clouds along the LOS. With a contribution from the CNM, the optical depth of the channel would be higher than that of the WNM-only LOS, and the spin temperature would be lower, moving data points upward from regime A in Figure 9. Since $T_B \sim T_s$ for an optically thick channel, which is only possible when the CNM dominates, the maximum brightness temperature would be limited to the maximum temperature of the CNM, $T_B \lesssim 200 \text{ K}$. The majority of both real and mock data points for high optical depth have brightness temperature close to the typical spin temperature of the CNM, $T_B \sim T_c \sim 80 \text{ K}$.

The reason for the lack of the observational points in regime B is related to the minimum optical depth of the CNM. The column density of a single CNM cloud is $\sim n_c l_c$, where n_c and l_c are the number density and size of the CNM cloud. The peak optical depth of the cloud is then

$$\tau_c = 0.17 \left(\frac{n_c}{10 \text{ cm}^{-3}} \right) \left(\frac{l_c}{\text{pc}} \right) \left(\frac{100 \text{ K}}{T_s} \right) \left(\frac{\text{km s}^{-1}}{\Delta v_{\text{FWHM}}} \right). \quad (20)$$

The brightness temperature of the CNM is then $T_B \sim \tau_c T_s \sim 17 \text{ K}$ for a typical small cloud. The high peak optical depth and brightness temperature of a single CNM cloud implies that observational points in regime B with $T_B < 10 \text{ K}$ and $T_s < 200 \text{ K}$ would either require a single CNM layer thinner than 1 pc (e.g., tiny scale atomic structure which is not resolved in our simulations; see Heiles 2007 for review) or far outer wings from multiple CNM clouds. A few data points are

observed in this regime in both real and mock observations, in contrast to the relatively sharp limit excluding regime A.

In Figures 9(b) and 10(b), we display the distributions of the synthetic line data without and with the WF effect, respectively, for different ranges of the harmonic mean “kinetic” temperature. The red, green, and blue contours denote CNM ($T_{k,\text{avg}}(v_{\text{ch}}) < 184$ K), UNM ($184 \text{ K} < T_{k,\text{avg}}(v_{\text{ch}}) < 5050$ K), and WNM ($5050 \text{ K} < T_{k,\text{avg}}(v_{\text{ch}})$), respectively. $T_{k,\text{avg}}(v_{\text{ch}})$ is defined analogously to Equation (11) for T_k . As we have seen in Figure 7 and 8, the majority of the UNM and WNM distributions (the innermost green and blue contours) are also completely mixed in $T_B(v_{\text{ch}}) - \tau(v_{\text{ch}})$ plane. This is in contrast to the sharply separated spin temperature distributions in Figures 9(a) and 10(a). The difference between contours of $T_{s,\text{obs}}(v_{\text{ch}})$ and $T_{k,\text{avg}}(v_{\text{ch}})$ again warns against naive use of the spin temperature as a proxy for the gas phase since there is not a one-to-one correspondence between $T_{s,\text{obs}}(v_{\text{ch}})$ and $T_{k,\text{avg}}(v_{\text{ch}})$ at all temperatures.

Using $T_{s,\text{obs}}(v_{\text{ch}})$, however, it is possible to separate the $T_B(v_{\text{ch}}) - \tau(v_{\text{ch}})$ plane into CNM-dominated, UNM-dominated, and UNM-WNM-mixed regimes. The CNM-dominated regime is obviously defined by $T_{s,\text{obs}}(v_{\text{ch}}) \lesssim 200$ K. As uncertainty in the WF parameters affects the spin temperature at low pressure (see Figure 2), the upper limit of the UNM-dominated regime is not well defined. From Figure 9(b), with no WF effect, a conservative definition of the UNM-dominated regime is $200 \text{ K} \lesssim T_{s,\text{obs}}(v_{\text{ch}}) \lesssim 1000$ K with $T_B(v_{\text{ch}}) \gtrsim 10$ K. From Figure 10(b), with WF effect at a high level included, the UNM-dominated regime is extended to $200 \text{ K} \lesssim T_{s,\text{obs}}(v_{\text{ch}}) \lesssim 2000$ K. In other words, for $\tau(v_{\text{ch}}) > 10^{-3}$ the one-to-one correspondence between $T_{s,\text{obs}}(v_{\text{ch}})$ and $T_{k,\text{avg}}(v_{\text{ch}})$ persists up to $T_{s,\text{obs}}(v_{\text{ch}}) \lesssim 1000$ K (without the WF effect) and $T_{s,\text{obs}}(v_{\text{ch}}) \lesssim 2000$ K (with the WF effect). Note that green points in the observational data are mostly in the UNM-dominated regime regardless of the WF effect. Therefore, the presence of the UNM is evident in the observed data, although the relative proportions of UNM and WNM in observed data is uncertain since the majority of the UNM is expected to be buried in the UNM-WNM-mixed regime.

4.2. Column Density of WNM-only LOSs

Recently, Kanekar et al. (2011) have proposed the existence of an H I column density threshold, $N_{\text{H},\text{lim}} = 2 \times 10^{20} \text{ cm}^{-2}$ for CNM to form, based on 21 cm emission and absorption line observations detailed in Roy et al. (2013a). They found that observed LOSs have a median spin temperature of $T_{s,\text{avg}} \sim 240$ K for $N_{\text{H}} > N_{\text{H},\text{lim}}$ and $T_{s,\text{avg}} > 1000$ K for $N_{\text{H}} \lesssim N_{\text{H},\text{lim}}$. This implies that the LOSs with $N_{\text{H}} > N_{\text{H},\text{lim}}$ consist of both CNM and WNM, while the WNM is predominant for the LOSs with $N_{\text{H}} \lesssim N_{\text{H},\text{lim}}$.

Here, we explain the observed CNM threshold behavior in the context of thermal and dynamical equilibrium in the ISM. As summarized in Section 2.1, our model disks are in thermal and dynamical equilibrium in an average sense (Kim et al. 2011, Paper I). Vertical dynamical equilibrium demands a balance between vertical pressure support and the weight of the gas. Also, thermal equilibrium for

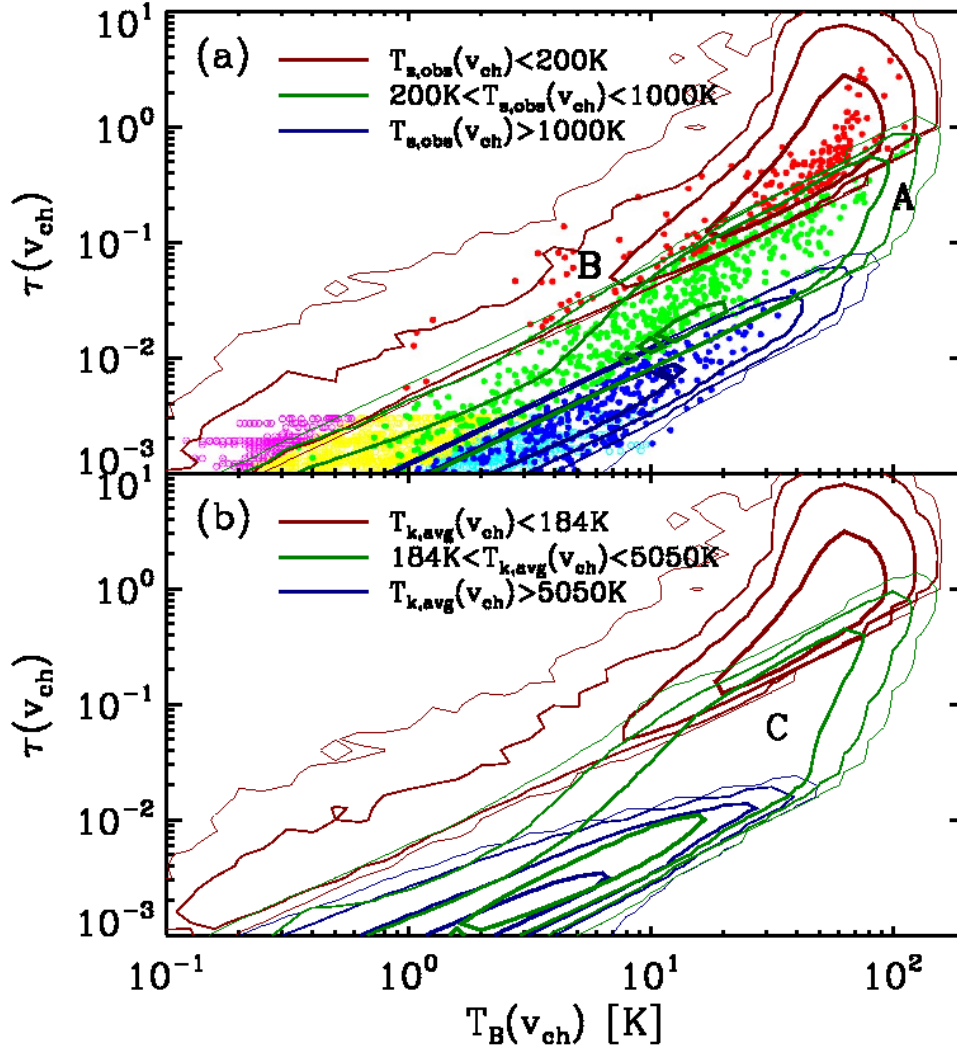


Fig. 9.— Distribution of the synthetic line data from simulation in the plane of the brightness temperature $T_B(v_{\text{ch}})$ and the optical depth $\tau(v_{\text{ch}})$ for all LOSs, channels, and snapshots of the QA10 model. The contour levels from outside (thinner) to inside (thicker) correspond to fractions of 10^{-5} , 10^{-4} , 10^{-3} , 10^{-2} in each temperature range. The red, green, and blue contours respectively denote different ranges of (a) spin temperature $T_{s,\text{obs}}(v_{\text{ch}})$ and (b) kinetic temperature $T_{k,\text{avg}}(v_{\text{ch}})$, as shown in the upper-left corner of each panel. The underlying data in (a) is from Figure 4 of Roy et al. (2013a). The red, green, and blue symbols denote observed spin temperature $T_s < 200$ K, $200 \text{ K} < T_s < 1000$ K, and $1000 \text{ K} < T_s$, respectively, for emission-detected channels. The magenta, yellow, and cyan symbols respectively denote the same temperature ranges for channels with non-detection. In (a), the observed data for emission-detected channels (filled circles) are very well enveloped by contours drawn from the synthetic line data: low $T_{s,\text{obs}}(v_{\text{ch}})$ gas lies at high $\tau(v_{\text{ch}})$ and $T_B(v_{\text{ch}})$, while gas with higher $T_{s,\text{obs}}(v_{\text{ch}})$ lies at lower $\tau(v_{\text{ch}})$ and $T_B(v_{\text{ch}})$. From (b), the region of high $T_B(v_{\text{ch}})$ and $\tau(v_{\text{ch}})$ corresponds to cold gas, and intermediate $T_B(v_{\text{ch}})$ and $\tau(v_{\text{ch}})$ to intermediate-temperature gas (as in region “C”), but gas at the lowest $T_B(v_{\text{ch}})$ and $\tau(v_{\text{ch}})$ can be either intermediate-temperature or warm.

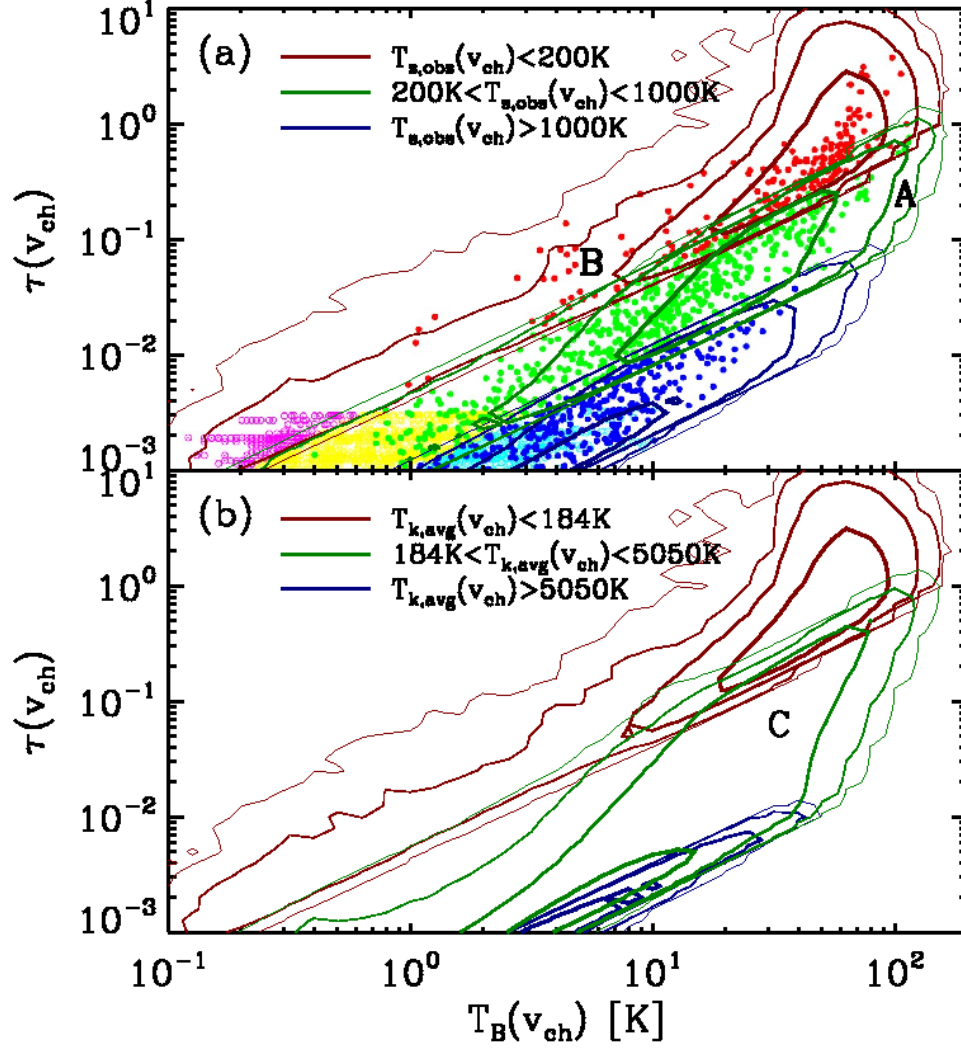


Fig. 10.— Same as Figure 9 but with the WF effect. In (a), overall distribution of the synthetic line data from simulation with respect to given spin temperature ranges are similar to Figure 10(a). In (b), the WNM (blue contours) is distributed in narrower region with lower $\tau(v_{ch})$ since the WF effect results in higher spin temperature (Figure 2(c) and (d)).

a two-phase neutral medium implies the midplane thermal pressure P_{th} lies between P_{min} and P_{max} ($P_{\text{th}} \sim \sqrt{P_{\text{min}} P_{\text{max}}}$ is a good first order approximation as in Wolfire et al. 2003; Ostriker et al. 2010). The equilibrium profile for a WNM-only vertical LOS can be approximated by a Gaussian profile with the midplane density of $n_w(0) = P_{\text{th}}/(1.1kT_w)$ and scale height of $H_w = \sigma_{z,w}/(4\pi G\rho_{\text{sd}})^{1/2}$, where T_w is the thermal equilibrium temperature at P_{th} for the WNM, $\sigma_{z,w} = (v_{\text{turb}}^2 + c_w^2)^{1/2}$ is the total (thermal and turbulent) vertical velocity dispersion of the WNM, and ρ_{sd} is the midplane density of stars and dark matter (which dominate the potential in the solar neighborhood). The one-sided WNM column density along a vertical LOS is

$$\begin{aligned} N_{\text{WNM}} &= \int_0^\infty n_w(z) dz = \sqrt{\frac{\pi}{2}} n_w(0) H_w = 1.14 \frac{P_{\text{th}} H_w}{k T_w} \\ &= 2.0 \times 10^{20} \text{ cm}^{-2} \left(\frac{P_{\text{th}}/k}{3000 \text{ cm}^{-3} \text{ K}} \right) \left(\frac{T_w}{7000 \text{ K}} \right)^{-1} \left(\frac{\sigma_{z,w}}{10 \text{ km s}^{-1}} \right) \left(\frac{\rho_{\text{sd}}}{0.1 \text{ M}_\odot \text{ pc}^{-3}} \right)^{-1/2} \quad (21) \end{aligned}$$

The reference values in the last expression are typical of the solar neighborhood; this gives N_{WNM} comparable to the $N_{\text{H,lim}}$ value reported in Kanekar et al. (2011). In Column (7) of Table 1, we list corresponding N_{WNM} calculated from the numerical outcomes of P_{th} and H_w in several numerical models representing a range of galactic conditions. For arbitrary galactic latitude b , the column density of a WNM-only LOS would be $N_{\text{WNM}}/\sin|b|$.

Figure 11 displays the distribution of $N_{\text{H}} \sin|b|$ in grey scale as a function of $\sin|b|$, drawn from our model QA10. The observed data points, plotted as filled circles with color denoting the spin temperature (taken from Roy et al. 2013a) follow the same general distribution as the mock observation data (grey scale). In order to quantify where the WNM dominates, we calculate the fraction of no-CNM LOS ($f_c = 0$) in each bin. From outside to inside, the contours demark no-CNM LOS fraction of $> 50\%$ (cyan), $> 70\%$ (green), and $> 90\%$ (magenta). The innermost magenta contour (more than 90% of LOSs lack CNM) envelopes the observed data points with high spin temperatures ($> 10^3 \text{ K}$). The horizontal dashed line marks N_{WNM} from Equation (21). Note that the spin temperatures of the observed data change systematically from small (CNM dominated) to large (UNM+WNM dominated) as $N_{\text{H}} \sin|b|$ becomes smaller. This is consistent with Figures 7 and 8, which show $\log T_{\text{s,obs}} > 3$ only for LOSs without CNM.

Since the disk is highly turbulent and time-variable, the midplane pressure of the WNM can be somewhat larger and smaller than the mean midplane pressure P_{th} . Thus, it is possible to have no-CNM LOSs with column density larger than $N_{\text{WNM}}/\sin|b|$. However, most LOSs, especially at small $|b|$, consist of both CNM and WNM, as seen in the region excluded from the contours in Figure 11. Where both WNM and CNM are present, $N_{\text{H}} \sin|b|$ will exceed N_{WNM} . We note, however, that the lowest values of $N_{\text{H}} \sin|b|$ from Roy et al. (2013a) appear in the regime that we expect will be WNM-dominated. We therefore suggest that the “cold threshold” column density seen by Kanekar et al. (2011) is not the manifestation of a minimum shielding column, but instead represents the vertical H I column with only WNM that is consistent with both thermal and dynamical equilibrium in the local Milky Way disk.

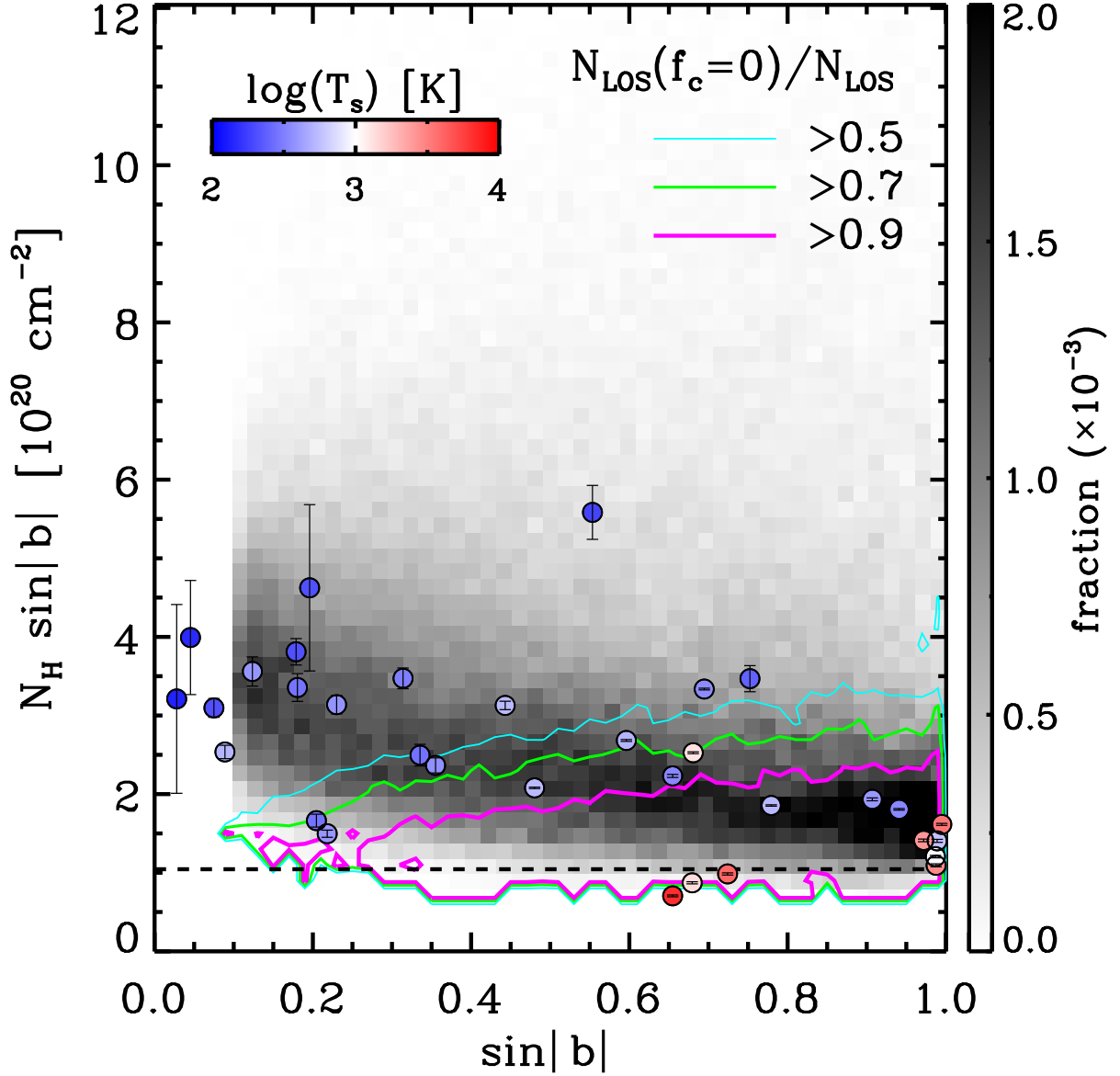


Fig. 11.— Distribution of the mock observation data of the column density (from model QA10) projected to the vertical LOS $N_H \sin|b|$ as a function of $\sin|b|$ for all LOSs and simulation snapshots. The grey scale displays the number fraction in each bin, with $N_H \sin|b|$ increasing at small $|b|$ because cold gas is concentrated more towards the midplane than warm gas. The contours indicate the fractions of the mock observation data in each bin that is no-CNM ($f_c = 0$) increasing from 0.5 (cyan) to 0.7 (green) to 0.9 (magenta). The symbols are observed data points from Roy et al. (2013a); the color of each symbol represents the logarithm of the spin temperature. The column density of the WNM-only LOS (see Equation (21)), N_{WNM} (using P_{th} and H_w for model QA10 from Table 1), is shown in the dashed line.

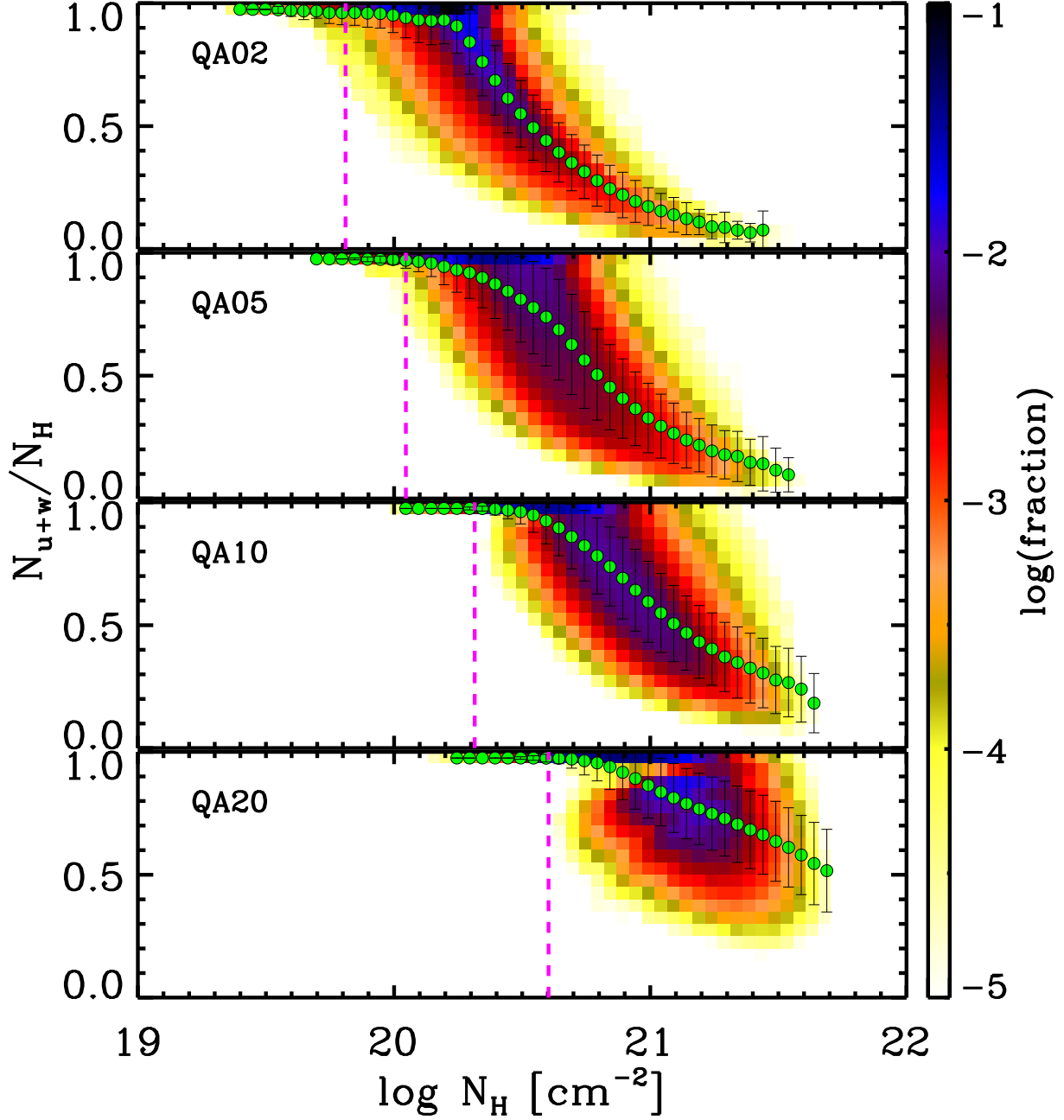


Fig. 12.— Distribution of the UNM+WNM mass fraction N_{u+w}/N_H as a function of total column density N_H for all vertical LOSs at all times in each simulation, for different galactic disk model environments (see Table 1). Here the column density is defined by integrating over the entire disk vertically in contrast to the half-thickness integration of Equation (21). The mean and standard deviation of the distribution in each N_H bin are shown as symbols and errorbars, respectively. The magenta dashed line shows the predicted value $2N_{\text{WNM}}$ for a WNM-only vertical column in thermal and dynamical equilibrium (see text). The decline below near-unity of the UNM+WNM mass fraction occurs at $\sim 2N_{\text{WNM}}$, as expected.

If external galaxies were observed with sufficiently high resolution and sensitivity, the column density of a WNM-only LOS would similarly vary with local disk conditions. In order to address this, we consider what an H I observer would see for different extragalactic ISM conditions as modeled by the set of simulations listed in Table 1. We vertically integrate the gas density through the entire disk to obtain the column density $N_{\text{H}} \equiv \int_{-\infty}^{\infty} n dz$. Note that this column density is twice that defined by Equation (10), which assumes an observer at the midplane. We also calculate the column density of the CNM (N_{c}) and the UNM *plus* WNM (N_{u+w}) in the same way. Here, we consider the UNM and WNM together since they are not distinguishable in H I line observations (see Figures 7 and 9).

Figure 12 displays the distribution of the UNM+WNM mass fraction N_{u+w}/N_{H} as a function of the total column density N_{H} . The color scale shows the distribution of the logarithmic number fraction for each of the simulations listed in Table 1. The symbols and errorbars respectively plot the mean and standard deviation of the distribution for each N_{H} bin. The vertical dashed line in each panel denotes the column density $2N_{\text{WNM}}$ for a WNM-only LOS under equilibrium conditions through the full disk thickness. For $N_{\text{H}} < 2N_{\text{WNM}}$, most of LOSs have N_{u+w}/N_{H} higher than 90%. Above this column density, LOSs are dominated by the two-phase mixture. Thus, $2N_{\text{WNM}}$ represents a lower limit on the total column for cold gas to be present.

The overall distribution and the threshold column density move toward higher N_{H} , as the total gas surface density increases from $2.5 \text{ M}_{\odot} \text{ pc}^{-2}$ to $20 \text{ M}_{\odot} \text{ pc}^{-2}$ (from QA02 to QA20 models). The self-regulated equilibrium model for atomic-dominated regions (Ostriker et al. 2010) predicts $P_{\text{th}} \propto \Sigma_{\text{SFR}} \propto \Sigma \sqrt{\rho_{\text{sd}}}$ and $H_w \propto 1/\sqrt{\rho_{\text{sd}}}$ if the ratio of thermal to total pressure, and the vertical velocity dispersion are approximately constant, as verified numerically for QA-series (Kim et al. 2011, Paper I). From Equation (21), we thus expect $N_{\text{WNM}} \propto P_{\text{th}} H_w \propto \Sigma$, explaining why N_{WNM} increases nearly linearly in the QA Series (see Table 1).

5. Summary and Discussion

The very first step to deduce the H I column density from 21 cm line observations is to convert the observed brightness temperature $T_{\text{B}}(l, b, v_{\text{ch}})$ to channel column density using Equation (13) or (14). Despite the importance of this first conversion step, the validity and uncertainty of the conversion methods have not previously been tested and quantified with realistic ISM models. At a minimum, a realistic ISM model should include multi-scale turbulence, as well as self-consistent density and temperature structure responding to the heating and cooling of the dynamic ISM. Our recent ISM simulations in Paper I include these ingredients, and thus provide a valuable testbed for evaluating 21 cm diagnostic techniques. Since our simulations are local, we limit our analysis to latitudes larger than $|b| > 5^{\circ}$ in which horizontal variations of the ISM play a lesser role.

Our main findings are summarized as follows.

1. By conducting mock observations toward random LOSs, we find that the observed spin temperature $T_{s,\text{obs}}(v_{\text{ch}})$ deduced from the brightness temperature and the optical depth (see Equation (12)) agrees very well with the true harmonic mean spin temperature $T_{s,\text{avg}}(v_{\text{ch}})$ (see Equation (11)). The agreement is within a factor of 1.5 even for the channel optical depths as large as $\tau(v_{\text{ch}}) \sim 10$. Since $T_{s,\text{obs}}(v_{\text{ch}})$ effectively assumes a single component along the LOS, this agreement implies that for the adopted velocity channel width of 1 km s^{-1} , there is limited LOS overlap of opaque CNM clouds. The agreement $T_{s,\text{avg}}(v_{\text{ch}}) \approx T_{s,\text{obs}}(v_{\text{ch}})$ in individual velocity channels also leads to good agreement between “observed” and “true” velocity-integrated properties, including $N_{\text{H,obs}} \approx N_{\text{H}}$ and $T_{s,\text{obs}} \approx T_{s,\text{avg}}$ (see Figure 6). $N_{\text{H,obs}}$ (see Equation 13) is also known as the “isothermal” estimator of the H I column density and widely used in observations (Dickey & Benson 1982; Chengalur et al. 2013). The “thin” column density is within a factor of ~ 0.7 of the “true” column density for $\tau_{\text{int}} < 10$, comparable to the observed ratio of “thin” to opacity-corrected column density $\sim 0.6 - 0.8$ (Dickey et al. 2003).
2. In our analysis, we calculate the spin temperature with and without the WF effect via the Ly- α resonant scattering, which provide upper and lower limits for the spin temperature of the WNM, respectively. As a consequence, we find the harmonic mean spin temperature (Equation 15) is limited to $T_{s,\text{obs}} \lesssim 2000 \text{ K}$ without the WF effect (see Figure 7) and $T_{s,\text{obs}} \lesssim 4000 \text{ K}$ with the WF effect (see Figure 8). There are a few absorption line observations of the WNM that have reported spin temperature up to $\sim 6000 \text{ K}$ (Carilli et al. 1998; Kanekar et al. 2003). The possible underestimation of the WNM spin temperature in our analysis (we omit collisional transitions due to electrons) might lead to higher optical depth of the WNM than in the real ISM. However, the optical depth is already quite small in the WNM, and we find a similar distribution in the space of $T_B(v_{\text{ch}})-\tau(v_{\text{ch}})-T_{s,\text{obs}}(v_{\text{ch}})$ to observations irrespective of the method for the spin temperature calculation (see Figures 9 and 10).
3. Our analysis shows that thermally-unstable and true warm gases appear in comparable proportions along all LOSs for most values of $T_{s,\text{obs}}$ (Figures 7 and 8). However, we do find that for $T_{s,\text{obs}}$ in the range $\sim 500 \text{ K} - 1000 \text{ K}$, UNM dominates over WNM. The detection of absorption with spin temperature in a range of $T_{s,\text{obs}} \sim 500 - 5000 \text{ K}$ (e.g., Carilli et al. 1998; Dwarakanath et al. 2002; Kanekar et al. 2003; Begum et al. 2010a) may imply the possible existence of thermally unstable gas. More definitive evidence for the UNM is given by a distribution of observational data in the space of $T_B(v_{\text{ch}})-\tau(v_{\text{ch}})-T_{s,\text{obs}}(v_{\text{ch}})$ (Figures 9 and 10). We show that the UNM alone populates the regime with $200 \text{ K} \lesssim T_{s,\text{obs}}(v_{\text{ch}}) \lesssim 1000 \text{ K}$ (near point “C” in Figure 9(b)) without the WF effect. With the WF effect, this regime can be extended to $200 \text{ K} \lesssim T_{s,\text{obs}}(v_{\text{ch}}) \lesssim 2000 \text{ K}$ (see Figure 10(b)). This is because the one-to-one correspondence between $T_{s,\text{obs}}(v_{\text{ch}})$ and $T_{k,\text{avg}}(v_{\text{ch}})$ persists up to at least $T_{s,\text{obs}}(v_{\text{ch}}) \lesssim 1000 \text{ K}$ and at best $T_{s,\text{obs}}(v_{\text{ch}}) \lesssim 2000 \text{ K}$ without and with WF effect, respectively. The presence of observational data points in this region strongly suggest that the presence of thermally unstable gas. Since the majority of the UNM and WNM occupy the low optical depth regime

$\tau(v_{\text{ch}}) \lesssim 10^{-2}$, with high spin temperature $T_{s,\text{obs}}(v_{\text{ch}}) \gtrsim 1000$ K where their distributions are completely mixed, however, the exact mass fractions of the UNM and WNM are difficult to derive from H I 21 cm observations.

4. While the spin temperature provides only limited ability to differentiate UNM and WNM, it is a very good probe of the CNM mass fraction. From Equation (16), the CNM mass fraction for moderate $T_{s,\text{obs}}$ is $f_{c,\text{obs}} \approx T_c/T_{s,\text{obs}}$. In our simulations, the median CNM temperature is 80 K, and Figure 7(a) shows that for LOSs with low spin temperature $T_{s,\text{obs}} \lesssim 400$ K, $f_{c,\text{obs}} \approx 80 \text{ K}/T_{s,\text{obs}}$ fits quite well. Because CNM temperature is not a single constant, however, there is an inherent uncertainty of about a factor of 2 in this result. Using Gaussian decomposition of emission/absorption lines, Dickey et al. (2003) have found the CNM temperature are in range of $40 \text{ K} \lesssim T_c \lesssim 100 \text{ K}$ with median value of ~ 65 K. Heiles & Troland (2003b) also have reported similar distributions with median and mass-weighted CNM temperatures of 48 K and 70 K, respectively.

Interesting results for the CNM mass fraction have recently been derived by emission/absorption line pairs from galactic plane surveys (Taylor et al. 2003; McClure-Griffiths et al. 2005; Stil et al. 2006). Dickey et al. (2009) have shown that the radial dependence of harmonic mean spin temperature in the Milky Way is nearly flat, implying that nearly constant CNM mass fraction out to 25 kpc. Our numerical models (Paper I; see also Kim et al. 2011) indeed find that mean CNM mass fraction varies only from ~ 0.2 to 0.4 for a wide range of conditions.

5. For a given equilibrium disk condition with midplane thermal pressure P_{th} and scale height of the WNM H_w , there is a maximum WNM-only vertical column density N_{WNM} (Equation (21)). This is comparable to the observed column density where a transition in $T_{s,\text{obs}}$ occurs, $N_{\text{H,lim}} \sim 2 \times 10^{20} \text{ cm}^{-2}$ (Kanekar et al. 2011). The detailed distributions of our mock observations shows that LOSs with projected column density $N_{\text{H}} \sin |b|$ smaller than N_{WNM} are highly likely to consist only of the WNM. N_{WNM} therefore represents well the transition column density from warm-dominated LOSs to LOSs with a two-phase mixture, for a wide range of model parameters (Figure 12).

We are grateful to the referee for an extremely helpful report, including encouragement to expand our discussion of the Wouthuyen-Field effect. This work was supported by grant AST0908185 from the National Science Foundation. The work of W.-T. K. was supported by the National Research Foundation of Korea (NRF) grant funded by the Korean government (MEST), No. 2010-0000712. The simulations used in this paper were performed by the facilities of the Shared Hierarchical Academic Research Computing Network (SHARCNET:www.sharcnet.ca) and Compute/Calcul Canada.

REFERENCES

- Allison, A. C., & Dalgarno, A. 1969, *ApJ*, 158, 423
- Audit, E., & Hennebelle, P. 2005, *A&A*, 433, 1
- Bajaja, E., Arnal, E. M., Larrarte, J. J., Morras, R., Pöppel, W. G. L., & Kalberla, P. M. W. 2005, *A&A*, 440, 767
- Begum, A., Stanimirović, S., Goss, W. M., Heiles, C., Pavkovich, A. S., & Hennebelle, P. 2010a, *ApJ*, 725, 1779
- Begum, A., et al. 2010b, *ApJ*, 722, 395
- Braun, R., & Walterbos, R. A. M. 1992, *ApJ*, 386, 120
- Burton, W. B. 1976, *ARA&A*, 14, 275
- Carilli, C. L., Dwarakanath, K. S., & Goss, W. M. 1998, *ApJ*, 502, L79
- Chengalur, J. N., Kanekar, N., & Roy, N. 2013, *MNRAS*, 432, 3074
- Dickey, J. M., & Benson, J. M. 1982, *AJ*, 87, 278
- Dickey, J. M., & Lockman, F. J. 1990, *ARA&A*, 28, 215
- Dickey, J. M., McClure-Griffiths, N. M., Gaensler, B. M., & Green, A. J. 2003, *ApJ*, 585, 801
- Dickey, J. M., Strasser, S., Gaensler, B. M., Haverkorn, M., Kavars, D., McClure-Griffiths, N. M., Stil, J., & Taylor, A. R. 2009, *ApJ*, 693, 1250
- Draine, B. T. 2011, *Physics of the Interstellar and Intergalactic Medium*
- Dwarakanath, K. S., Carilli, C. L., & Goss, W. M. 2002, *ApJ*, 567, 940
- Ewen, H. I., & Purcell, E. M. 1951, *Nature*, 168, 356
- Field, G. B. 1958, *Proceedings of the IRE*, 46, 240
- . 1959, *ApJ*, 129, 551
- Field, G. B., Goldsmith, D. W., & Habing, H. J. 1969, *ApJ*, 155, L149
- Furlanetto, S. R., Oh, S. P., & Briggs, F. H. 2006, *Phys. Rep.*, 433, 181
- Gould, R. J. 1994, *ApJ*, 423, 522
- Hagen, J. P., Lilley, A. E., & McClain, E. F. 1955, *ApJ*, 122, 361
- Hartmann, D., & Burton, W. B. 1997, *Atlas of Galactic Neutral Hydrogen*
- Heiles, C. 2007, in *Astronomical Society of the Pacific Conference Series*, Vol. 365, *SINS - Small Ionized and Neutral Structures in the Diffuse Interstellar Medium*, ed. M. Haverkorn & W. M. Goss, 3
- Heiles, C., & Troland, T. H. 2003a, *ApJS*, 145, 329
- . 2003b, *ApJ*, 586, 1067
- Hennebelle, P., & Audit, E. 2007, *A&A*, 465, 431

- Hill, A. S., Jounge, M. R., Mac Low, M.-M., Benjamin, R. A., Haffner, L. M., Klingenberg, C., & Waagan, K. 2012, *ApJ*, 750, 104
- Kalberla, P. M. W., Burton, W. B., Hartmann, D., Arnal, E. M., Bajaja, E., Morras, R., & Pöppel, W. G. L. 2005, *A&A*, 440, 775
- Kalberla, P. M. W., & Dedes, L. 2008, *A&A*, 487, 951
- Kalberla, P. M. W., Dedes, L., Kerp, J., & Haud, U. 2007, *A&A*, 469, 511
- Kalberla, P. M. W., & Kerp, J. 2009, *ARA&A*, 47, 27
- Kanekar, N., Braun, R., & Roy, N. 2011, *ApJ*, 737, L33
- Kanekar, N., Subrahmanyam, R., Chengalur, J. N., & Safouris, V. 2003, *MNRAS*, 346, L57
- Kim, C.-G., Kim, W.-T., & Ostriker, E. C. 2008, *ApJ*, 681, 1148
- . 2010, *ApJ*, 720, 1454
- . 2011, *ApJ*, 743, 25
- Kim, C.-G., Ostriker, E. C., & Kim, W.-T. 2013, *ApJ*, 776, 1
- Koyama, H., & Ostriker, E. C. 2009, *ApJ*, 693, 1346
- Kulkarni, S. R., & Heiles, C. 1987, in *Astrophysics and Space Science Library*, Vol. 134, *Interstellar Processes*, ed. D. J. Hollenbach & H. A. Thronson, Jr., 87–122
- Lazareff, B. 1975, *A&A*, 42, 25
- Levine, E. S., Blitz, L., & Heiles, C. 2006a, *Science*, 312, 1773
- . 2006b, *ApJ*, 643, 881
- Liszt, H. 2001, *A&A*, 371, 698
- Mac Low, M.-M., Balsara, D. S., Kim, J., & de Avillez, M. A. 2005, *ApJ*, 626, 864
- McClure-Griffiths, N. M., Dickey, J. M., Gaensler, B. M., Green, A. J., Haverkorn, M., & Strasser, S. 2005, *ApJS*, 158, 178
- Muller, C. A., & Oort, J. H. 1951, *Nature*, 168, 357
- Ostriker, E. C., McKee, C. F., & Leroy, A. K. 2010, *ApJ*, 721, 975
- Ostriker, E. C., & Shetty, R. 2011, *ApJ*, 731, 41
- Payne, H. E., Salpeter, E. E., & Terzian, Y. 1983, *ApJ*, 272, 540
- Piontek, R. A., & Ostriker, E. C. 2007, *ApJ*, 663, 183
- Roy, N., Kanekar, N., Braun, R., & Chengalur, J. N. 2013a, *MNRAS*, 436, 2352
- Roy, N., Kanekar, N., & Chengalur, J. N. 2013b, *MNRAS*, 436, 2366
- Saury, E., Miville-Deschênes, M.-A., Hennebelle, P., Audit, E., & Schmidt, W. 2013, *ArXiv e-prints*
- Seifried, D., Schmidt, W., & Niemeyer, J. C. 2011, *A&A*, 526, A14
- Shetty, R., & Ostriker, E. C. 2012, *ApJ*, 754, 2
- Spitzer, L. 1978, *Physical processes in the interstellar medium*

- Stil, J. M., et al. 2006, AJ, 132, 1158
- Taylor, A. R., et al. 2003, AJ, 125, 3145
- Vázquez-Semadeni, E., Gazol, A., & Scalo, J. 2000, ApJ, 540, 271
- Wolfire, M. G., Hollenbach, D., McKee, C. F., Tielens, A. G. G. M., & Bakes, E. L. O. 1995, ApJ, 443, 152
- Wolfire, M. G., McKee, C. F., Hollenbach, D., & Tielens, A. G. G. M. 2003, ApJ, 587, 278
- Wouthuysen, S. A. 1952, AJ, 57, 31
- Zygelman, B. 2005, ApJ, 622, 1356